NTNU – Trondheim
Norwegian University of
Science and Technology

Pump-probe experiments of multicrystalline silicon for solar cell applications

Lisa Grav Henriksen

Master of Science in Physics and Mathematics
Submission date: July 2012
Supervisor: Ursula Gibson, IFY
Co-supervisor: Ulf Österberg, IET

Norwegian University of Science and Technology
Department of Physics

Abstract

In order to make cost effective solar cells from mc-Si materials, the negative contributions from defects and impurities should be reduced. The analysis of the photogenerated carrier properties is therefore of great importance for characterising carrier processes and hence, for improving the material performance.

In this work, pump-probe measurement of a range of silicon wafers have been performed, using an ultrafast laser of 800 nm wavelength and 85 fs pulses. The optical response in the samples were analysed by measuring the reflected probe beam initial transient.

The purpose of this theses was to explore the use of pump-probe experiment to study carrier dynamics in mc-Si. Measurements of single c-Si samples were used as a basis for developing good experimental skills as well as achieving knowledge about carrier dynamics in c-Si. The initial $\Delta R/R$ was studied for a range of input parameters, aiming to characterise important contributions to the measurements.
The effects of passivation has been studied, indicating a significant contribution to $\Delta R/R$. Etching off the passivated layer of an oxide (SiO2) wafer, showed a radically increased in pump beam reflectivity, from 9% to 32%, and a reduced $DeltaR/R$ from 47×10^{-6} to 37×10^{-6} was be observed. Analysis has showed that incident angle may be chose such that the pump reflection loss is at a minimum for the given passivation thickness.

The final results showed a $\Delta R/R$ is in the range of $(14-41) \times 10^{-6}$ for bare c-Si, and $(47-171) \times 10^{-6}$ for passivated c-Si wafers.

Ultrafast initial recovery has been observed for mc-Si samples, and attributed to trapping of carriers. Decay times in the range of 1-6 ps are deduced and trapping densities are found as $(1.3 - 4.3) \times 10^{18}\ cm^{-3}$, which is in the same order as the excitation densities.

A methodology for using pump-probe measurements to analyse mc-Si samples is established, and the technique is used in characterising the observed defect states, which is of great interest for improving solar cell materials.

Sammendrag

For å kunne utvikle priseffektive solceller fra mc-Si prøver, må de negative bidragene fra defekter og urenheter reduseres. Analyse av de eksiterte ladningenes egenskaper vil da være svært viktig for å kunne karakterisere prosesser som finner sted, og for slik å kunne foredre materialets ytelse.

I dette arbeidet er pump-probe eksperimenter av ulike silisium prøver blitt gjennomført, ved bruk av en superrask laser med 800 nm bølgelendge og 85 fs pulser. Den optiske responsen i prøvene er analysert ved å måle den reflekterte probe strålens umiddelbare endring etter eksitasjon.

Formålet med denne oppgaven var å utforske bruken av pump-probe eksperiment for å studere ladningsdynamikken i mc-Si. Målinger av singel c-Si prøver har vært bruks som et grunnlag for å utvikle en god eksperimentell teknikk, i tillegg til å oppnå kunnskap om ladnings dynamikken i c-Si. Then umiddelbare $\Delta R/R$ har blitt undersøkt for en rekke innputt parametere, med det mål å kunne karakterisere viktige bidrag til våre målingene.

Effektene av passivering ble studert ved å utføre målingen på SiO2 og Si3N4 prøver. Passiveringslaget på en SiO2 prøve ble etset bort, for å se hvordan dette på virket resultatene. Utslaget viste en stor økning i refleksjonen fra pump strålen, fra 9% til 32%, og en reduksjon i $\Delta R/R$ verdi fra $47 \times 10^{-6}\ V$ til $37 \times 10^{-6}\ V$. Videre analyse har vist at innkommende vinkel kan justeres slik at pump refleksjonen er på en minumum, gitt passiveringslagets tykkelse.

Sluttresultatene viste en $\Delta R/R$ i størrelsen $(14 - 41) \times 10^{-6}\ V$ for bar c-Si, og $(47 - 171) \times 10^{-6}\ V$ for passivert c-Si prøver.

En umiddelbare gjennoppretting av det reflekterte probe signalet har blitt observert for mc-Si prøver, som kan tilskrives ladnings feller i materialet. En rask redusjon med stigetid på 1-6 ps har blitt funnet, med en felletetthet på $(1.3 - 4.3) \times 10^{18}\ cm^{-3}$, som er i samme størrelsesorden som eksitasjonstettheten.

Metodikk for bruk av pum-probe målinger for å analysere mc-Si prøver er etablert i dette arbeidet, og teknikken er brukt for å karakterisere de observerte defektene. Dette er av stor interesse for å kunne forbedre solcelle materialer.

Acknowledgment

I would like to thank my supervisor Professor Ulf Österberg for all the support and help he has been given me during this semester, both in the lab and at his office. He has always been available for questions and taken his time to discuss my work whenever I needed advices or new solutions to unexpected problems. He has been a good motivator with commitment to this work and care for his students.

I would also like to thank my supervisor Professor Ursula Gibson for all the help she has given me along the way. Discussions with her have really made my work move forward and brought new experimental techniques into my master work. She has provided the wafers I've used in this theses, and put me in contact with the right person when external experiment has been performed.

I would like to thank Chiara Modanese at Material Science for trusting my experimental skills and lending me mc-Si wafers. I would also like to thank Erlend Nordstrand at the same department, for teaching me polishing of wafers and being so helpful and patient. I would also like to thank Ph.D. student Fredrik Martinsen for taking his time to help me out with HF-etching a wafer in Nanolab.

I would like to thank Wilhelm Dall at Sintef Trondheim for performing EBSD mapping of a mc-Si wafer and taking me through each step of this process. I would also like to thank Rune Søndenå at IFE at Kjeller for carrying out Microwave Conductive Decay measurments and for being so flexible when we had to change our plans.

Finally, I would like to thank my friend and fellow student Hans Skjeie for the the time we spent in the lab together, and for the support and care he has given throughout this semester.

Contents

Acknowledgment . . . v

1 **Introduction** **1**

2 **Basic concepts of semiconductors** **3**

2.1 Energy band gap . . . 3

2.2 Crystal structure . . . 4

2.3 Generation and recombination . . . 4

2.3.1 Thermal generation . . . 5

2.3.2 Photon absorption . . . 5

2.4 Indirect and direct transition . . . 6

2.4.1 Absorption coefficient . . . 8

2.5 Silicon . . . 8

2.5.1 Multicrystalline Si . . . 10

2.6 Doping . . . 10

2.7 p-n junction . . . 11

3 **Semiconductor dynamics** **13**

3.1 Ultrashort time domain . . . 13

3.2 Recombination processes . . . 16

3.3 Recombination processes in silicon . . . 17

3.3.1 Trap states in mc-Si . . . 17

3.3.2 Surface states and passivation . . . 18

4 Optical properties of semiconductors **19**
4.1 Dielectric function and refractive index 20
4.2 Reflection 21
4.3 Drude model 24
4.4 Conductivity 26
4.5 Intraband contribution 27

5 Experimental setup **29**
5.1 Basic pump-probe technique 29
5.2 Lasers 31
5.3 Lock-in amplifier 35
5.4 Chopper Frequency 36
5.5 Laser beam properties 37
5.5.1 Pump beam 37
5.5.2 Number of photons 39
5.5.3 Probe beam 39
5.5.4 Beam polarizations 39
5.6 Experimental preparation 40
5.7 Samples 41
5.8 Probe reflection in equilibrium 42
5.9 Crystal orientations 42
5.10 Other experimental techniques 43
5.10.1 EBSD mapping 43
5.10.2 THz-TDS 44
5.10.3 Microwave Photoconductive Decay 45
5.10.4 Reflectivity measurements 45

6 Results and discussion **47**
6.1 Pump reflection 47
6.2 Bare single crystalline Si 47
6.3 Passivated single c-Si 50
6.3.1 Pump-probe results 50
6.3.2 Microwave lifetime measurement 52

6.3.3 Passivation thickness 52
6.3.4 Removing passivation layer 55
6.3.5 Incident angle and passivation layer thickness 55
6.4 Crystal orientation 57
6.4.1 Variations in measurements 57
6.5 Quantum efficiency 60
6.6 Multicrystalline Si 61
6.6.1 Measurements of mc1 61
6.6.2 Measurements of mc2 64
6.6.3 Measurements of mc3 and mc4 64
6.6.4 Causes of defects 65
6.7 Conductivity analysis 67

7 Conclusion **71**

8 Future work **73**

Appendices **75**

A Lock-in amplifier **77**
A.1 Lock-in theory 77
A.2 Procedure to reset the lock-in amplifier 78

References **81**

List of Figures

2.1 A schematic presentation of a cubic crystal, showing different crystal directions in the lattice. Illustration taken from in [35] 4

2.2 A schematic presentation of the density of state function g(E), the Fermi Dirac distribution function f(E), the energy distribution n(E) at T=0 and for T>0. The shaded area shows the electron distribution. Illustration taken from in [35] 6

2.3 A schematic presentation of indirect and direct band gaps. Illustration taken from [35]. 7

2.4 A schematic presentation of the energy band diagram for Silicon. Illustration based on figure in [21] 9

2.5 Illustrates how two neighbouring crystal grain may give rise to disordered crystal structure, such as unpaired electrons which are not included in the bonding. Illustration based on figure in [21] 10

2.6 Shows how the Fermi level is shifted for p- and n-type doping. Illustration based on figure in [21] 11

3.1 A schematic diagram illustrating the photoexcitation of a semiconductor and the main relaxation processes. Initally after photon absorption, the carriers can be describe by a delta function distribution in momentum and energy space (a). Through scattering events, the momentum randomizes within tens of femtoseconds (b). Carrier-carrier scattering thermalizes carriers into a Fermi-Dirac distribution with temperatures T_e and T_h greater than lattice temperature T_L (c). As time evolves the hot carriers lose their excess kinetic energy while attempting to reach thermal equilibrium with the lattice through optical phonon scattering (d). Illustration taken from [24]. 15

3.2 The surface of a silicon crystal, with passivated dangling bonds. Illustration taken from [35]. 18

5.1 Schematic presentation of the pump and probe pulses. The probe pulse has a time delay τ relative to the pump. 30

5.2 Experimental setup for pump-probe measurements detecting the reflected probe signal. 30

5.3 Illustration of the concepts behind a mode-locked laser. The upper figure shows the time domain description of a mode-locked laser, with the carrier envelope phase $\Delta\phi$. The lower figure shows the frequency domain description, with a pulse repetition rate f_{rep} and a comb offset due to pulse shifts f_0. Illustration taken from [14]. . . . 31

5.4 Optical layout of the Ti: Sapphire laser Solstice, with Mai Tai SP seed and Empower pump. Illustration provided by the manufacturer. 33

5.5 Schematics of the pulse stretcher used in the process called chirp. Stretching is important to prevent damage in the amplifier crystal. The reverse process can then be performed to recover the high power pulse. 34

5.6 The measured signal displayed on the autocorrelator, showing a FWHM of 130 fs. The output power is 3.4 W. 35

5.7 Generic timing for chopper. 36

5.8 Experimental setup for orthogonal pump and probe polarizations. A waveplate is used to rotate the probe polarization perpendicular to the pump polarization, and a polarizer limits the scattered pump light into the detector. 40

5.9 Illustration of a cubic crystal structure. A (100) wafer has a normal <100> perpendicular to the <110> directions. 43

5.10 A schematic arrangement of a EBSD setup. Illustration taken from [39]. 44

5.11 A schematic arrangement of spectral reflectivity measurement. A white light source sends light towards the sample and the reflected signal is detected by fibres in the reflection probe. 45

6.1 Pump-probe measurement of the bare samples bn0 and bp0 49

6.2 Pump probe measurements of the passivated wafers. The pump polarization is along the <110> direction and the probe polarization is parallel to the pump. 51

6.3 Microwave lifetime map of the oxidized n-doped Si wafer. The circles present the areas exposed to the pump beam. The average carrier lifetime across the wafer is found to 2.8 μs. 52

6.4 Presents the spectral reflectivity: found from measurements, calculated with the thickness given by the manufacturer and calculated with an adjusted thickness for a better fit to the measured result. 53

6.5 Presents the calculated reflectivity for pump incident angle 5° and probe incident angle 45°, over a range of passivation layer thicknesses. The results are shown for passivated nitride wafers Si3N4 and oxidized SiO2 wafers. 56

6.6 $\Delta R/R$ results from a series of nine pump-probe measurements performed at the exact same spot of wafer ox1, carried out right after each other. 58

6.7 Illustration of the measured $\Delta R/R$ values obtained for each wafer, when the wafer was removed and then put back in the setup. 59

6.8 Illustration of the Gaussian shape pump pulse. 59
6.9 Pump-probe measurements performed within a grain on sample mc1. 62
6.10 Pump-probe measurement performed within grain number 2 on wafer mc1. 63
6.11 Pump-probe measurements of grain boundaries on sample mc1. 64
6.12 Pump-probe measurements of sample mc2. 65
6.13 Pump-probe measurements of the samples mc3 and mc4. 65
6.14 Results from pump-probe measurement performed on a repolished wafer. The probe beam polarization is parallel to the pump beam. 66
6.15 EBSD mapping of sample mc1. The circles presents areas where pump-probe measurements have been performed. 67

A.1 Shows a picture of the lock-in settings during experiment. 79

List of Tables

3.1 Fundamental processes in semiconductors. Table taken from [24]. 14

4.1 Delta R/R dependence of the carrier density (n, p) [cm^{-3}] for s- and p-polarized light and for n- and p-doped materials 26

5.1 Table of silicon samples used in the experiment. Showing the properties: type of doping, crystal orientation, wafer thickness and resistivity. 41

5.2 Measured probe reflection in % from each sample, with probe polarization parallel and perpendicular to the pump polarization. Incident angle is 45°. 42

6.1 Measured pump reflection in % from each sample. Incident angle is 5° and the pump beam polarisation is horizontal. 48

6.2 Measured $\Delta R/R$ and calculated excitation density for pump-probe measurements on bare and passivated single crystalline Si wafers. The table presents the crystal plane parallel to the pump beam polarization and the probe polarization relative to the pump. The excitation density is calculated for parallel pump and probe polarizations. 50

6.3 Presents the passivated layer thickness given by the manufacturer and the adjusted thickness to fit experimental results. The error in the value given the manufacturer is shown. 54

6.4 Spectral reflectivity for 800 nm light, with the calculated and measured values. . . 55

6.5 Results from pump-probe measurements performed on mc-Si wafers, within grains (WG) and at grain boundaries (GB). The table presents the values for $\Delta R/R$, excitation densities, fast decay time, the reflection recovery (in %) and the trapping density. 63

6.6 Estimated static conductivity σ_{dc} and mobility μ from THz TDS results. The values for carrier density n_{eq}, collision time τ and ω_p used in the estimation are also presented. 68

Chapter 1

Introduction

The world experienced a tremendous increase in global energy consumption during the 20th century. The large demand for energy has mainly been covered by burning fossil energy sources; oil, gas and coal. However, fossil fuels are limited resources, with an estimated lifetime of only a few decades for oil and gas. As the fast growing energy consumption will continue into the 21st century, the decreasing resources of fossil energy urges the need for alternative energy sources [21].

In 2008, oil, gas and coal accounted for 81% of the global energy supply, showing the large dependence on fossil fuels. Only 12% represented all the renewable energy sources; hydro, geothermal, wind, solar and biofuel [5]. Today we know more about the long-term consequences of burning fossil fuels, and how large amount of CO2 released into the atmosphere may cause significant climate changes on Earth. The growing awareness of the need for other energy sources to replace fossil fuels, has triggered the interest for environmental-friendly and sustainable energy sources [38].

In the 1970s, western countries with a large oil-dependent energy market experienced an oil-crisis and a lack in energy supply. This became the driving force for developing alternative energy sources, and our understanding of solar cell technology is rooted in this period. The pollution-free, unlimited and available energy from the sun received much attention and might explain why photovoltaic power has been one of the fastest growing renewable energy technology since the 1970s. The advantage were many: reliable, easy to use, lack of noise and no emission, which lead to an incredible development. In late 1990s the solar cell production expanded with 15-25% a year, resulting in reduced costs and the opportunity for new photovoltaic markets to open [7].

The processes in a solar cell is based on solar photovoltaic energy conversion, where electrical energy is generated from light energy. The physics behind this is based on quantum theory, stating that light contains packets of energy, called photons. The energy of a photon only depends upon the wavelength, or the color, of the light. If the photon energy is sufficient, it may break out an electron which is bound into a solid, and bring it to a level of higher energy. The electron can now be regarded as a free carrier, because it is more free to move in this energy level and not bound to the solid. However, relatively quickly it relaxes back to its ground state and recombine in the solid.

Alexandre-Edmond Becquerel was the first to report an observation of light breaking free an electron in a solid. He observed that light produced a current between electrodes immersed in a electrolyte in 1839. Later in 1905, Einstein was the first to described this phenomena, known as the photoelectric effect. This forms the basis for the photovoltaic (PV) technology, and started the development of solar cells. A photovoltaic device is made in such a way that it can exploit the excited free electrons before they relax back to their initial position. When the electrons are free to move, they are pulled away by a built-in asymmetry and fed into an external circuit. The new distribution of charged carriers creates a potential difference, or an electromotive force, that drives the exited electrons through the external circuit and generates an electrical current [21].

Through out the solar cell history, silicon (Si) has been the most important material for more than 30 years, and it still is today. In year 2010, 90 % of all the photovoltaic installations were based on crystalline silicon technology. Silicon has a range of advantages compared to other materials; sustainable, no toxicity, available and with a long lifetime. Despite the unique advantages and bright future for use in solar cells, the limiting factor and main drawback today is the production cost. After 30 years of technology improvements and costs reductions, the material costs are still the main barrier for a large global PV market to develop [7].

The energy consumption in the production of silicon solar cells today is dominated by the process of purifying and crystallizing the base silicon. By reducing these processes, the production costs will decrease significantly. Silicon wafers are mainly produced by solar-optimized growth method, resulting in crystalline Si (c-Si) with low defect density. Using another less energy consuming method will produce multi-crystalline Si (mc-Si) wafers, with grains and higher defect density. Solar grade silicon with larger impurity concentration, has a cost estimation of 10-20 $/kg compared to the electric grade price of 50-70 $/kg [7]. This indicates a large potential for material cost reductions and market growth. Consequently, a new approach has developed; to make cost effective solar cells from low cost, but rich impurities feedstock.

The high defect density in multicrystalline (mc-Si) compared to monocrystalline Si, is result of large number of grain boundaries and defects within grains. Grain boundaries are sources of defects and act as recombination center for free carriers. Carriers might also be captured into deep or shallow traps in the material. Hence, high defect and impurity densities will reduce the lifetime of carriers, and lower the solar cell efficiency. This makes it hard to achieve a solar cell of high performance. To overcome this challenge and improve the efficiency of mc-Si for use in solar cells, it is essential to have detailed knowledge of the carrier dynamics in the material [12].

This work will therefore investigate properties and carrier dynamics of c-Si and mc-Si samples using optical pump-probe technique. In the experiment an intense laser pulse is used to excite free carriers in a sample. A much weaker probe is delayed with respect to the pump, and monitors the changes in optical properties in the sample. By using a range of time-delays, the experiment can give a dynamical picture of the free carriers' behaviour and important information about the materials.

Chapter 2

Basic concepts of semiconductors

In chapter 1, the fundamental principle of photoelectric effect was introduced and the basics of a photovoltaic converter was described. In this chapter, we will introduce the basic knowledge about semiconductors and their most important properties for use in photovoltaic applications.

2.1 Energy band gap

The absorption of a photon upgrades an electron to a level of higher energy, to an excited state, in the material. The photovoltaic device collects the excited electrons and exploit their potential energy. For the electrons to maintain in the higher energy state long enough to be collected, the energy bands are separated by a *band gap*, E_g. The extra potential energy gained from the photon absorption, allows the electrons to be pulled away from their point of creation and available as electrical energy. However, only photons with energy sufficient to cross the band gap can promote an electron to a higher energy state. Hence, the band gap of a material is of great important for photovoltaics.
Semiconductors and insulators are materials with an energy band gap, but only some of them are suitable for photovoltaic applications. The band gap of insulators is too big for the visible light to bridge the gap so the absorption of a phonon is not permitted. The band gap is related lowest possible wavelength that can be absorbed by the material. Semiconductors can be describes as materials with band gap from roughly 0.5-3 eV which allows the absorption of visible light. This is the most important property of a semiconductor, which makes it possible to use in photovoltaic technology.

When atoms are brought together and form bonds with each other, the molecular orbitals are arranged slightly different from each atomic energy level, resulting in a slit in energy levels. When many atoms form a solid, each atomic energy level is split into a wide range of energy levels. These levels are close to each other in energy and make a band of allowed energy states. In a semiconductor, the bands for different molecular orbital in the solid do not overlap, which establishes the characteristic energy band gap between the bands.
The energy bands may be occupied or unoccupied. The highest occupied band is called the *valence band* at energy E_v, and contains the valence electrons. The lowest unoccupied band is called the

conducting band at lies at the energy level E_c. The energy bands can be empty, partly full or completely full and determines the properties of the solid. The band gap is the energy difference between the valence and the conduction band [21, 35].

2.2 Crystal structure

The atoms is a crystalline solids are arranged in periodic system where basic arrangement of atoms that is repeated through the solid. This periodicity can be described by identical groups of atoms which are repeated trough the crystal. Such a group is called the *basis* and is defined by a symmetric array of points in the *crystal lattice*. The crystal structure depends upon the number of valence electrons, as it will try to minimize the total energy in the structure. Since silicon atom contains four available electrons, the vacant electrons will bond to four neighbour atoms when forming a crystal basis, aiming to include all valence electron in bonding.

It might be convenient to referring to planes and directions within the crystal lattice. A lattice coordinate system, called *Miller indices*, describes a set of parallel planes in the lattice. Figure 2.1 illustrates the crystal directions in a cubic lattice [18, 35].

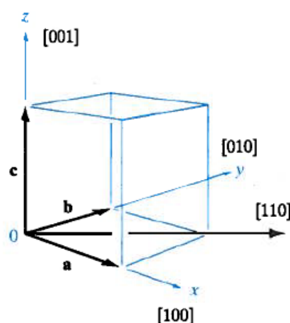

Figure 2.1: A schematic presentation of a cubic crystal, showing different crystal directions in the lattice. Illustration taken from in [35]

2.3 Generation and recombination

Generation is an excitation event which requires an input energy, and increases the number of free carriers in the conduction band. The input energy may be supplied by vibrational energy of light(photon), of the lattice(phonons) or from kinetic energy from other carriers.

A photovoltaic device is based on the important principle that when a generation process occurs, an equivalent recombination process must take place. Recombination reduces the number of free carriers through the decay of an electron to a lower energy level. The excess energy can be released through three main recombination processes: as a photon (*radiative* recombination), as

heat through a phonon (*non-radiative* recombination) or as kinetic energy to other carriers (*Auger* recombination). These processes are described in details in chapter XXX.

When an electron is excited to a higher energy level, a positively charged vacancy is left in the lower energy state. This empty state is refereed to as a hole and an electron-hole pair is created. The vacant state may be occupied by another electron close by, and makes it possible for electrons to move to neighbouring states. Since the number of electrons is large compared to few holes, it is easier to think in terms of holes moving in the opposite direction [35].

2.3.1 Thermal generation

At absolute zero, a semiconductor is a solid with a completely full valence band and an empty conduction band. The electrons occupy the lowest available energy levels, up to a state where the energy is called the *Fermi energy*, E_F. There is no charge transport since there are no available states for the electrons to move.

As the temperature rises, the vibrational kinetic energy in the lattice makes it possible for some of the electrons to move across the band gap, through thermal generation, and into an energy state above E_F. In the same way, excited electrons can thermally recombine to vacant states at a lower energy level. The generation and recombination rates increases as the temperature rises. However, in thermal equilibrium, the generation and recombination are balanced and the number of free electrons in the conduction band equals the number of vacant states in the valence band. Hence, the distribution of carriers has settled and E_F is the same for all points [35, 21].

In equilibrium, the distribution of electrons can be described by Fermi Dirac statics. Together with the electron internal energy k_BT for the given temperature T, where k_B is Boltzmann's constant, and the Fermi energy E_F, the Fermi Dirac distribution function $f_0(E, E_F, T)$ can be derived. It gives the average probability for an electron state at energy E to be occupied at a given temperature T,

$$f_0(E, E_F, T) = \frac{1}{e^{(E-E_F)/k_BT} + 1} \tag{2.1}$$

Figure 2.2 illustrates the density of state function g(E) together with the Fermi Dirac distribution for T=0 and for T>0. The energy distribution is also shown for absolute zero and for T>0.

2.3.2 Photon absorption

For solar cells and photovoltaic devices, the main generation process is optical and the energy is provided by the absorption of a photon.
Light contains photons with energy $E = h * \nu$. If the incoming photon has an energy larger than the band gap of the material, $E > E_g$, the photon can be absorbed by the lattice, giving an electron energy enough to make a transition across band gap. The excited electron and the free hole are able to conduct electricity, a phenomena is called *photoconductivity*.

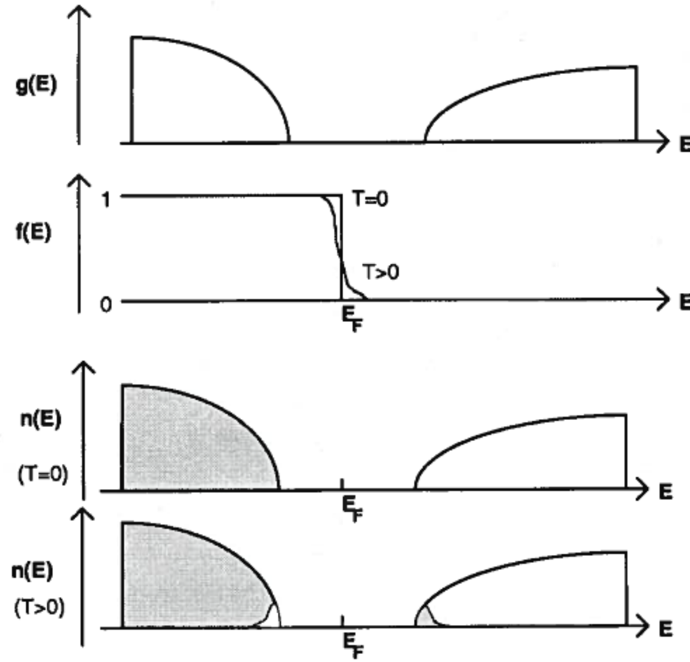

Figure 2.2: A schematic presentation of the density of state function g(E), the Fermi Dirac distribution function f(E), the energy distribution n(E) at T=0 and for T>0. The shaded area shows the electron distribution. Illustration taken from in [35]

Photogeneration is the generation of free electrons and holes as a result of photon absorption. The generated electron density in CB is denoted n and the density of holes in VB is denoted by p.

Quantum efficiency(QE) is an important measure for a solar cell performance. QE is the rate of the incoming photons that produce charged carriers in the material. For a solar cell, QE is the ratio of the number of collected electrons contributing to a current, to the number of incoming photon. Hence, the quantum efficiency describes the material's sensitivity to light, which is a key parameter for photovoltaic devices. QE depends upon the absorption coefficient and the efficiency of charge collection in the semiconductor material. The external QE(EQE) includes the total number of incoming photons, and is given by

$$EQE = \frac{number\ of\ collected\ electron}{number\ of\ incoming\ photons} \tag{2.2}$$

2.4 Indirect and direct transition

A semiconductor may have a direct or an indirect band gap. For a direct band gap, see figure 2.3a, the valence band maximum and conduction band minimum are located right above each other in k-space. This means that the crystal momentum vector **k** describing the maximum energy state in valence band is the same as the **k**-vector describing the energy state at the conduction band minimum. A transition between the two energy bands can be done through absorption or emission of a photon, without a change in momentum. For an indirect band gap, in figure 2.3b, the energy

states in the valence band and the conduction band are described by two different **k**-vectors, **k** and **k'**. Since crystal momentum must be conserved, an indirect transition requires a change in the momentum vector **k** [2, 42].

The existence of finite temperature in the lattice, creates lattice vibrations which are quantized

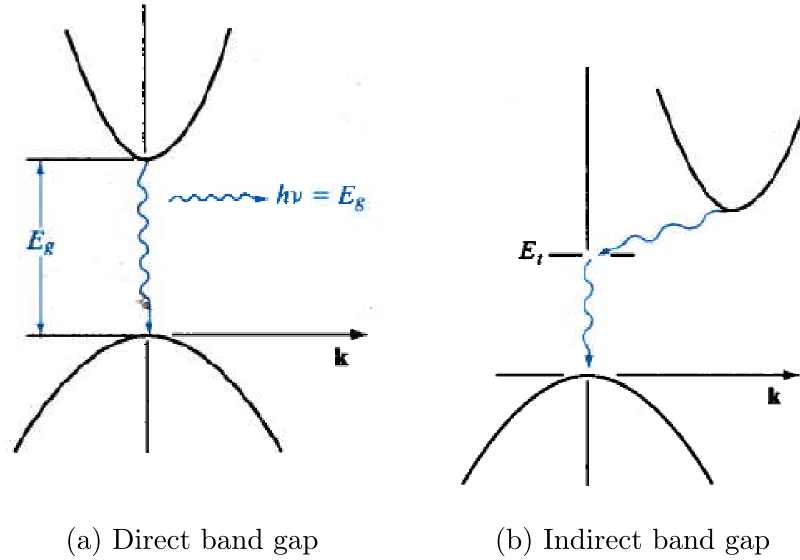

(a) Direct band gap (b) Indirect band gap

Figure 2.3: A schematic presentation of indirect and direct band gaps. Illustration taken from [35].

and called phonons. An electron with high energy can create or reduce lattice vibrations, in other words create or absorb a phonon. The phonon density will depend on temperature; at higher temperatures the lattice vibrations increase and make the phonon density higher.

Photons with energy $\hbar\omega$, do not contain crystal momentum and cannot transform the **k**-vector. Hence, the only way of changing the crystal momentum is through interactions with phonons of energy $E_p = \hbar\omega_p$ and momentum $\hbar\mathbf{k_p}$. The phonon momentum must be equal the difference between valence band and conduction band momentum, so $\mathbf{k'} - \mathbf{k} = \mathbf{k_p}$. From conservation of energy, the phonon energy required for an indirect transition to occurs is

$$E_p = E_c(\mathbf{k'}) - E_v(\mathbf{k}) - \hbar\omega \tag{2.3}$$

A transision through an indirect band gap is only possible if a phonon of suitable $\mathbf{k_p}$ is available. Hence, the transition rate is determined by the number of phonons available. According to Bose-Einstein statistics, the probability of finding a phonon of energy E_p is given as $\frac{1}{e^{E_p/k_BT}-1}$.

Compared to direct transition, indirect excitation is less likely to happen because it is dependent on the phonon density and hence the temperature. Consequently, a photon with energy close to the band gap can travel further into an indirect band gap material before being absorbed than a direct band gap material.

2.4.1 Absorption coefficient

Studying the absorption spectrum of a semiconductor can give a lot of information about the distribution of states and possible transitions. A photon is absorbed by an electron which is excited up to a higher energy state, and by looking at the changes in the transited radiation, one can get important information about the semiconductor [2].

The absorption coefficient in materials will vary depending on whether the material has a direct and an indirect band gap. The formulas for the respective absorption coefficient are derived in [42] and stated below. These expressions are valid for photon energies larger, but not much larger than the band gap, and ignores the contribution from exciton; electrical attraction between electrons and holes that are just created.

The absorption coefficient can be calculated through the simple expression for direct and indirect band gaps

$$\alpha = \frac{1}{d} ln \frac{(1-R)^2}{T} \tag{2.4}$$

where d is the thickness of the sample and T and R are the optical transmittance and reflectance for the material at normal incident.

The absorption coefficient for direct bandgap is given as

$$\alpha \approx \frac{q^2 x_{vc}^2 (2m_r)^{3/2}}{\lambda_0 \epsilon_0 \hbar^3 n} \tag{2.5}$$

where ν is the frequency of the light, m_r is the reduced mass and is given as $m_r = \frac{m*_h m*_e}{m*_h + m*_e}$, n is the real part of the refractive index and x_{vd} is a matrix element with same order of magnitude as the lattice constant.

The indirect absorption coefficient is expressed in [42] as

$$\alpha \propto \frac{(h\nu + E_p - E_g)^2}{\exp(\frac{E_p}{kT}) - 1} + \frac{(h\nu - E_p - E_g)^2}{1 - \exp(-\frac{E_p}{kT})} \tag{2.6}$$

where $E_p = h\nu_{\mathbf{p}}$ is the phonon assisted energy that is needed in the indirect transition, k is Boltzmann's constant and T is the thermodynamic temperature.

2.5 Silicon

Silicon is a material in the IV group, which is characterized by the tetrahedral crystal structure. The indirect band gap, from the highest point in the valence band to the lowest point in the conduction band, is only 1.1 eV at room temperature. The direct band gap in Si is separated by 3 eV, and only light with an corresponding photon energy, e.g. blue light, can interact in a direct transition. Figure 5.10 shows the band diagram for silicon, with indicated arrows for direct and indirect excitation. A pump pulse with 800 nm wavelength (red light) has a photon energy equal 1.55 eV and will excite electrons from states near the valence band maximum at the Brillouin zone center Γ, to states close to the conduction band minimum in the X valley. These two vallyes are located six k-space positions away from each other and an additional change in k-vector is required through phonon absorption [29, 42].

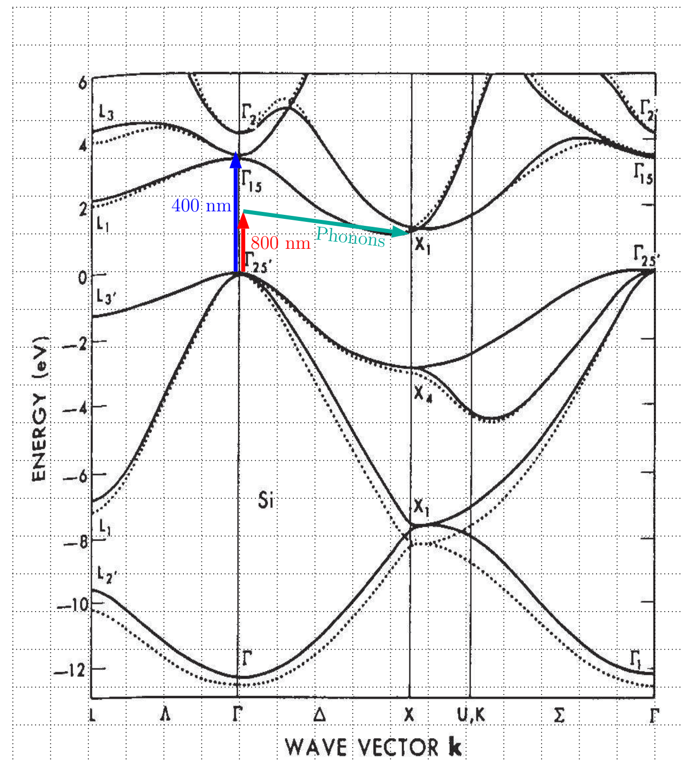

Figure 2.4: A schematic presentation of the energy band diagram for Silicon. Illustration based on figure in [21]

2.5.1 Multicrystalline Si

A multicrystalline material is created by crystallites or 'grains' with a size of 0.1-10 cm, and with a random orientation to each other. One grain is crystalline silicon with the same effective band structure as single crystalline silicon. However, mc-Si typically contains a larger impurity density and crystal defects any occur at the grain boundaries. Figure reffig:mc-struc illustrates how two neighbouring crystal structures at the grain boundaries may give rise to carriers which are not included in the bonding. The may grain boundaries may therefore have a large influence on the carrier dynamics in the material.

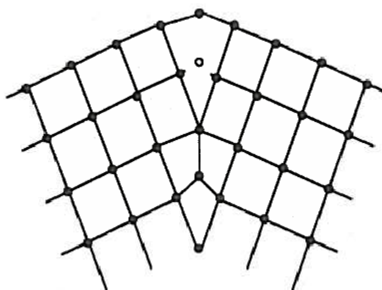

Figure 2.5: Illustrates how two neighbouring crystal grain may give rise to disordered crystal structure, such as unpaired electrons which are not included in the bonding. Illustration based on figure in [21]

2.6 Doping

Doping is a process of introducing impurity atoms to the material. The impurities make bonds to the atoms in the perfect crystal, and change the energy state distribution in that area. If the energy levels of the impurities lies within the band gap of the semiconductor, the electronic properties of the material might be changed.

A *n type doped* material describes a semiconductor which is doped to increase the density of electrons compared to the density of holes. The impurities used in n type doping are called donors atoms because they donate an extra electron to the lattice. The donor level creates an occupied state within the band gap. One example of n type doping, is silicon doped with phosphoros, which has five valence electrons while silicon only has four available bonds. The excess electron is not strongly bond to the crystal lattice, and can relatively easily break free, leaving the donor atom positively charged.

Similar, a p type semiconductor is doped to increase the density of positive charge holes relative to the electron density. This is done my introducing acceptor impurities, which has a too few valence electrons and creates an acceptor level for electrons. The most common p type doping used, is silicon doped with boron atoms, which only has three valence electrons. The unpaired

bond will try to remove a valence electron from other atoms, to complete all four bonds, and resulting in free hole which is able to move. The donor impurities is located close to the valence band.

During the doping process, the Fermi level is adjusted due to the new energy state distributions created. For a n type semiconductor at $T = 0$, all the donor states are now filled and the Fermi level must lie between the donor level and E_c. While for a p doped material, all the acceptor states are empty at $T = 0$ and the Fermi level must lie between the acceptor level and E_v. This is shown in figure 2.6.

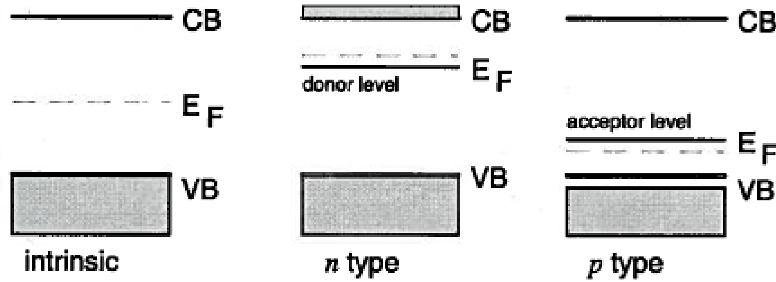

Figure 2.6: Shows how the Fermi level is shifted for p- and n-type doping. Illustration based on figure in [21]

2.7 p-n junction

A key parameter in photovoltic energy conversion, is charge separation. This requires some kind of driving force which must be built in to the device. When an n-type and a p-type semiconductor are brought together, the selective doping of the different sides leads to potential barrier between the regions. Hence, the excess donor electrons from the n-type material cross to the p-type material, and vice versa. A layer of fixed charge is left when the carrier diffusion over to the other side, due to the ionised impurity atoms on each side. This space charge sets up an electrostatic field across the junction, opposing further diffusion. A steady state is reached when the diffusion of majority carriers across the junction is balance by the drift of minority carriers due to the electrostatic field. The transition region between the n-type and the p-type semiconductors is called the space-charge region or depletion region. For the minority carriers to generate an electrical current, the diffusion length should be long enough for the carriers to cross the junction before recombining with a carrier of opposite charge. The minority carrier lifetime τ is a measure of the average time a minority carrier will diffuse before recombining [21]. Hence, the number of generated carriers and the carrier lifetimes, are important parameter for a photovoltaic device.

Chapter 3

Semiconductor dynamics

This chapter will give a brief overview of some of the relevant microscopic processes taking place in the ultrashort time domain in a semiconductor material, after a laser pulse excitation.

3.1 Ultrashort time domain

Under equilibrium conditions, free electrons and holes in a semiconductor are described by Fermi-Dirac statistics, while phonons are distributed according to Bose-Einstein statistics. Energy and momentum are exchanged through carrier-carrier and carrier-phonon interactions and in equilibrium, these interactions create a common temperature among the distributions. However, when the semiconductor is exposed to an external perturbation, such as a laser pulse, the carrier and phonon distributions may have different temperature and thermal states.

A laser pulse with a photon energy $\hbar\omega$ larger than the energy gap E_g in the semiconductor, will generate a large nonequilibrium carrier density. The excess kinetic energy, $h\omega - E_g$, will raise the carrier temperature. Depending on the incident pulse fluence and the photon energy, the generated carrier density and carrier temperature may increase several orders of magnitude above the equilibrium values, which will affect the interaction among carriers and phonons radically. The carries undergo temporal changes with characteristic times as the system evolves towards equilibrium. The main relaxation processes and the corresponding time are shown in table 3.1.

After an optical excitation, the absorbed photon energy is transferred fully to the carriers, which produces specific momentum states as well as new carrier temperatures. The first relaxation processes to occur is momentum relaxation, which happens through elastic and inelastic scattering processes from carrier-carrier and carrier-phonon collisions. Momentum relaxation takes place on a femtosecond time scale with a corresponding relaxation time denoted τ_m. In addition, the carrier-carrier scattering of electrons and holes thermalizes the carrier temperatures and allows the systems to be described by Fermi-Dirac statistics again, with electron and hole temperatures of T_e and T_h.

Table 3.1: Fundamental processes in semiconductors. Table taken from [24].

Microscopic process	**Characteristic time(s)**
Carrier-carrier scattering	$10^{-15} - 10^{-12}$
Intervalley scattering	$\geq 10^{-14}$
Intravalley scattering	$\sim 10^{-13}$
Carrier-optical phonon thermalization	$\geq 10^{-12}$
Optical phonon-acoustic phonon interaction	$\sim 10^{-11}$
Carrier diffusion (0.1 μm)	$\sim 10^{-11}$
Auger recombination (carrier density $10^{20} cm^{-3}$)	$\sim 10^{-10}$
Radiative recombination	$\geq 10^{-9}$
Lattice heat diffusion (1 μm)	$\sim 10^{-8}$

Parallel to momemtum relaxation, the scattering events give rise to energy relaxation. This happens through interaction with phonons, and emission of optical phonons. Electrons in the conduction band may interact with phonons of large wave-vectors which might scatter the electron into side valleys and contributes to intervalley scattering. For phonons with a small wave-vector, the electrons and holes might be scattered to another position within the valley, contributing to intravalley scattering.

The generated optical phonons may interact with each other through multiphonon processes. Phonon-phonon interactions results in thermalization towards the lattice temperature. Interactions between carriers and phonons is present for times greater than, or in the range of, picoseconds. Depending on the excitation energy, multiphonon interaction may occur for a longer period of time. This accumulation will result in a large population of non-equilibrium phonons, also called hot phonons, which possess higher temperature than the surrounding lattice. Electrons might reabsorb these phonons and hence increase the energy relaxation time. Eventually, the hot carriers will reach equilibrium with the lattice temperature.

Excess kinetic energy during the excitation process contributes to an increased carrier temperature. The result is a a larger carrier diffusion coefficient and hence, a faster carrier diffusion. The effective mass for electrons is much lighter than the effective mass for holes, resulting in different carrier diffusion, $\mu_e \neg \mu_p$. The increased diffusion will last for a few picoseconds until the carriers lose their kinetic energy and the system returns to equilibrium. The spatial diffusion of carriers do however persist for a period of nanoseconds.

The effective mass for electrons is much lighter than the effective mass for holes which means that electrons will possess most of the excess kinetic energy. Hence, the thermal distribution of holes and electrons will be different and have to be considered as separate systems.

The carrier density determines the time domain for which the carrier-carrier recombination takes place. For higher densities, the recombination process will occur on a shorter time scale relative to the initial excitation. For high densities, it will be on a time scale greater than 100 ps. The process is called Auger recombination and is the only recombination process within the ultrashort time domain.

Within the ultrashort time domain, the average momentum relaxes to zero and the carrier temperature relaxes to the lattice temperature. The relaxation time of carrier momentum and energy is dependent on the number and behaviour of the scattering processes involved. Figure 3.1 summaries the main carrier dynamics taking place within the first picosenconds after an optical excitation [24, 29, 3].

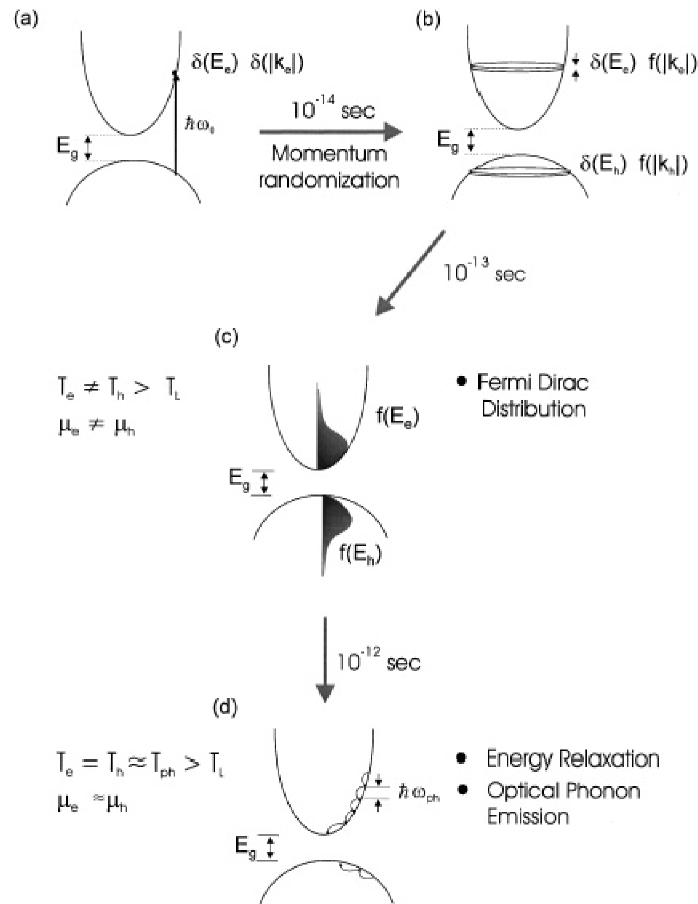

Figure 3.1: A schematic diagram illustrating the photoexcitation of a semiconductor and the main relaxation processes. Initally after photon absorption, the carriers can be describe by a delta function distribution in momentum and energy space (a). Through scattering events, the momentum randomizes within tens of femtoseconds (b). Carrier-carrier scattering thermalizes carriers into a Fermi-Dirac distribution with temperatures T_e and T_h greater than lattice temperature T_L (c). As time evolves the hot carriers lose their excess kinetic energy while attempting to reach thermal equilibrium with the lattice through optical phonon scattering (d). Illustration taken from [24].

3.2 Recombination processes

For times longer than the ultrashort time domain (more than hundreds of picoseconds), carrier recombination becomes the dominating process. Through bulk and surface recombination event the excited electrons are transferred back to valence band, where it recombines with a corresponding hole. As mentioned in chapter 2, there are several recombination mechanisms which play an import part in a photovoltaic device which will be described in the following sections. Recombination processes might be divided into two group: unavoidable and avoidable recombination mechanisms. The unavoidable processes are due to the fundamental physical processes in the semiconductor, while the avoidable mechanisms are caused by impurities or defects in the material [21, 29].

Among the unavoidable processes, *radiative recombination* is a result from optical generation and the corresponding spontaneous emission. Radiative recombination causes an electron to make a transition from the conduction band to the valence band, by emitting an photon with the same amount of kinetic energy, $E_c - E_v$, made available through recombination. Radiative recombination is important for direct band gap materials where the absorption is strong.

Auger recombination is another unavoidable recombination process which includes the interaction between carriers, causing one of them to recombine to a lower energy level. The collision between two similar carriers, electrons or holes, may result in an recombination across the band gab for one of them, and an excitation to a level of higher energy for the second carrier. The kinetic energy released through recombination, is transferred to the other carrier by increasing its energy. As the excited carrier relaxes to the conduction band edge, the excess energy is given up as heat. The carrier radiative lifetime is denoted τ_{rad} and represents the time for how long the carriers can maintain in the conduction band before the recombine through the radiative mechanism.

Auger processes are most important in low band gap materials with high carrier densities. In highly doped semicondutors, or at high temperatures, the large carrier density increases the carrier-carrier scattering and the Auger recombination might become the dominant recombination process. The carrier lifetime for Auger recombination is denoted τ_{aug} and is strongly dependent on doping concentrations.

In real semiconductor, the dominating recombination processes are results of defect or trap states in the band gap of the semiconductor. Chapter 2 provides further details about the possible defects causing trap states in the semiconductor. Excited carriers in the conduction band may relax to a trap state of lower energy. The energy loss through relaxation is transferred as heat. The carrier may be released by thermal excitation to a higher energy level. Typically trap states located in the middle of the band gap act as recombination centres where a trapped electron can recombine with a hole of opposite charge.

The recombination through single traps are describe Shockley Read Hall (SRH) recombination. SRH recombination may the dominated process for undoped materials, where the number of electrons n is similar to the number of holes p. The carrier lifetime associated with SRH mechanism, τ_{SRH}, depends upon the density of traps and where they are located in the band gap.

Trap assisted SHR recombination is particular relevant at the semiconductor surface. This is because surface states increase the trap density in this region. The recombination rate will depend on the density of surface defects. In real semiconductors, trap assisted recombination will be the dominating recombination mechanism. The resulting carrier lifetime will be the sum of the contribution from radiative, Auger and SRH recombination. This can be written as

$$\frac{1}{\tau} = \frac{1}{\frac{1}{\tau_{SHR}} + \frac{1}{\tau_{rad}} + \frac{1}{\tau_{aug}}} \tag{3.1}$$

3.3 Recombination processes in silicon

In lightly doped silicon, where the electron and hole concentrations are similar, the trap assisted Shocley Read Hall (SRH) recombination dominates. The minority lifetime is expected to decrease as the doping concentration increases, indicating that the number of traps varies with the doping concentration. In a lightly p-doped silicon the SRH typically contributes to a carrier lifetime of 10 μs, while a lightly n-doped silicon material has a lifetime of 1 μs. In highly doped Si, the Auger recombination is the dominant process, while the radiative recombination lifetime in Si is so long and never dominates the recombination process. Since Si is an indirect band gap material the radiative lifetime is typically in the order of milliseconds [21].

3.3.1 Trap states in mc-Si

The different crystal orientations between neighbouring grains are sources of defects. Dislocation, disordered bond angle and misplaced atoms are structures that may occur at the intersection between two crystal structures, thus at a boundary between two grains. External impurities may arise from growth of the material, and are typically located at the grain boundaries. The crystal defects and impurities give rise to additional states which are not ruled by the symmetry of the crystal. These states may have energies located within the band gap, and are referred to as intra band gap states or trap states, since carriers may get trapped in such states.

There are shallow and deep trap states, depending on where they are location in the band gap. Shallow traps refers to the trap states close to conduction or the valence band. A trap state located near the conduction band, will act as an acceptor and create a trap state for electrons, while a trap state close to the valence band will act as detonators and trap holes. Deep traps are located near the center of the band gap and can trap both electrons and holes. Such states have long release time, and the probability for the carriers to recombine is high. Consequently, deep traps acts as recombination centres within the band gap.

In a p-doped multicrystalline Si, the trap states located at the grain boundaries will trap a majority of free generated holes. As the accumulation of positive charges increases, a positive charged plane will be created at the interface of two grains. As a result, two negative charged layers arise on each side of the positive plane. An electrostatic force is set up and a potential barrier is created, pushing the positive charged majority carriers away, and pulling the minority charges towards the

grain boundary. In this region the negative charged minority carriers can easily recombine with the trapped holes. Hence, the grain boundaries are reducing the minority carrier diffusion length and their lifetime, as the act as recombination centres within the band gap. So the grain boundary recombination can be added to the recombination processes, and might be the dominating process for low doping concentrations and a high grain boundary density.

3.3.2 Surface states and passivation

The atoms in the bulk of a silicon crystal are bond to each other and form the tetrahedral crystal structure. However, at the surface of the silicon crystal the atoms are not able to fill all the bonds with neighbouring atoms. Each atom at the surface will therefore have one missing bond compared to the bulk atoms, and the missing bond is called *dangling bond*. This is illustrated in figure 3.2a. Hence, the surface silicon atoms are bonded to only three rather than four neighbouring Si atoms, leaving one valence orbital unpaired. The energy level of the under-coordinated Si atom will move in to the band gap and act as a deep trap in the material [17].
The density of defects states, effectively trap states, can be reduced by saturating the dangling bonds with atoms that form bond with the unpaired Si atoms. Hydrogen has the ability to diffuse in silicon and to create bond to dangling bonds, and thus passivate the defects. Passivation improves the material properties as defect concentration is reduced and the associated defect states of dangling bonds are eliminated. Oxidation of crystalline Si, may reduce the dangling bonds, since they form bonds to the oxygen atoms. A passivation process can introduce hydrogen atoms into the Si, which reduces the concentration of dangling bonds. An illustration of this, is shown in figure 3.2b and 3.2c.

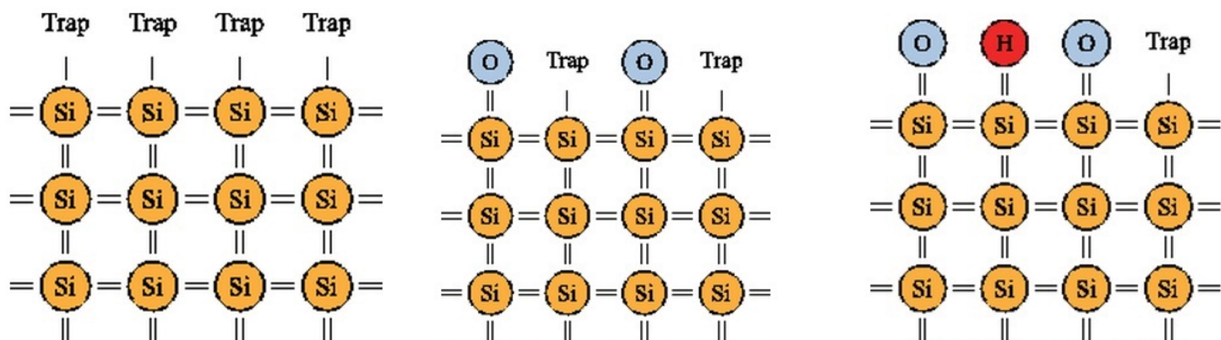

(a) Unpaired dangling bonds. (b) Si passivated with oxide. (c) Si passivated with hydrogen.

Figure 3.2: The surface of a silicon crystal, with passivated dangling bonds. Illustration taken from [35].

Chapter 4

Optical properties of semiconductors

When a electromagnetic field, like a laser pulse, propagates through a medium, the medium respond to this. The applied E-file will result in electric dipole moments of the atoms in the material and the sum of these interactions can be represented by the polarization P. For a incoming electric field with a filed strength comparable to the atomic binding force in the material, the incoming field might break free a significant number of bound electrons from the atomic binding. The absorption in the material, α, affects the electric field intensity through the material and the number of excited electrons. The density of generated carriers can be expressed

$$n(x,t) = n_0(t)e^{-\alpha d}$$

where d is the penetration depth in the material and n_0 is the photoexcited carrier concentration at the surface. The number of free carriers influence the optical properties in the semiconductor, such as the refractive index $\tilde{n}$, the dielectric function $\tilde{\epsilon}$ and the material reflectivity R [13].

Hence, the complex refractive index $\tilde{n}$ will experience a perturbation from its initial value $\tilde{n}_0$ to

$$\tilde{n} = \tilde{n}_0 + \Delta\tilde{n}(t)$$

where $\Delta\tilde{n}(t)$ is the time dependent perturbation caused by the incoming light pulse. As the generated free carriers recombine to their initial energy states, through varies processes described in Chapter 2, the perturbation is reduced and $\tilde{n}$ will reach its initial value [40].

The absorption coefficient will also experience a change from its initial value α_0 when an incoming light pulse interacts with the material

$$\alpha = \alpha_0 + \Delta\alpha(t)$$

The transmittance and the reflectivity of the material vary with the absorption through the sample and the refractive index at the surface. Before the perturbation, the reflected probe signal R_0 and the transmitted probe signal T_0 may be measured. After the excitation by an intense pulse, changes in $\tilde{n}$ and α will give rise to small changes in the transmitted and the reflected signals,

$$R = R_0 + \Delta R(t)$$

$$T = T_0 + \Delta T(t)$$

The relation between ΔR and ΔT is given in reference [32] as $\Delta T/T = \Delta R/R$.

Detecting the time-varying reflected and transmitted signals, can give us information about how $\tilde{n}$ and α are varying with time. This is of great importance as it provides detailed knowledge about the carrier dynamics in the semiconductor.

4.1 Dielectric function and refractive index

The complex dielectric function of Si at a wavelength 800 nm is given in [29, 9] as

$$\tilde{\epsilon} = \epsilon_r + i\epsilon_i = 13.656 + i0.048 \tag{4.1}$$

We can see that $Re(\tilde{\epsilon}) \gg Im(\hat{\epsilon})$. In our experiment the variation in dielectric function $\Delta\tilde{\epsilon}$ is small, in other words $|\Delta\tilde{\epsilon}| \ll |\tilde{\epsilon}|$ and $Re(\Delta\tilde{\epsilon}) \geq Im(\Delta\tilde{\epsilon})$. The resulting imaginary part of the dielectric function will be very small compared to the real part and we can only considering the real part of the change, $Re(\Delta\tilde{\epsilon})$, when calculating the resulting change in reflectivity [29].

The refractive index $\tilde{n}$ is related to $\tilde{\epsilon}$ through the expression [28]

$$\tilde{n} = \tilde{\epsilon}^{1/2} \tag{4.2}$$

The complex refractive index is given by the the Kramers-Kronig relation [26]

$$\tilde{n}(\omega) = n_r(\omega) + in_i(\omega) \tag{4.3}$$

For wavelength 800 nm, the complex refractive index of silicon is $\tilde{n} = 3.695 + i0.0065$. The real part of the refractive index is related to the speed of light in the medium, the imaginary part is directly related to the absorption of light through the material. The imaginary part also gives information about the complex conductivity of carriers in matter [15].

A change in the refractive index means variations in the real part, $Re(\Delta\tilde{n}) = \Delta n_r$, and in the imaginary part $Im(\Delta\tilde{n}) = \Delta n_i$. From equation 4.2 we can see that the our assumption of only considering the contribution from $Re(\Delta\tilde{\epsilon})$, is equivalent to only considering the real part contribution, Δn_r, of the refractive index. Hence, reflectivity changes can be described by the contribution from the real part of the refractive index change only.

The absorption coefficient is related to the imaginary part of $\tilde{n}$, and only differs from n_i by a constant factor [15]

$$\alpha = \frac{2\omega n_i}{c} \tag{4.4}$$

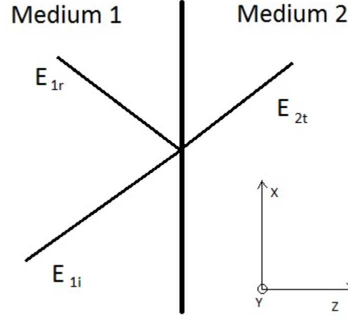

4.2 Reflection

An incoming monochromatic electromagnetic wave with wavevector k, can be expressed by the magnetic- electromagnetic amplitude

$$H = H_0 e^{i(kz-\omega t} \tag{4.5}$$

$$E = E_0 e^{i(kz-\omega t} \tag{4.6}$$

At an intersection between two mediums with different refractive index, electric field is given by the incoming and reflected electric field in medium one and the transmitted electric field in medium two, as shown i figure **??**. So, in medium one

$$E_1 = E_{1i} + E_{1r} \tag{4.7}$$

and in medium two

$$E_2 = E_{2t} \tag{4.8}$$

Maxwell's equations for the transversal electromagnetic waves with complex wavevector k are given by

$$k \times E = -\omega B \tag{4.9}$$

$$k \times H = \omega D \tag{4.10}$$

$$k \cdot D = 0 \tag{4.11}$$

$$k \cdot B = 0 \tag{4.12}$$

H and the electromagnetic field E are given by

$$H = \frac{1}{\omega \mu_0} k \times E \tag{4.13}$$

$$E = -\frac{1}{\omega \epsilon} k \times H \tag{4.14}$$

$$E_{yi} + E_{yr} = E_{yt} \tag{4.15}$$

$$H_{zi} + H_{zr} = H_{zt} \tag{4.16}$$

$$k_{xi}E_{yi} + k_{xr}E_{yr} = k_{xt}E_{yt} \tag{4.17}$$

$$k_{xi} = k_{xt} \tag{4.18}$$

$$k_{xi} = -k_{xr} \tag{4.19}$$

The reflection and transmission coefficients are be given by

$$r = \frac{E_{yr}}{E_{yi}} \tag{4.20}$$

$$t = \frac{E_{yt}}{E_{yi}} \tag{4.21}$$

They are related to each other by the

$$1 + r = t \tag{4.22}$$

Applying this to the wavevector k_z

$$k_{zi} + rk_{zr} = tk_{zt} \tag{4.23}$$

From figure **??** it can be seen that $k_{zi} = -k_{zr}$. This gives an expression for the reflection coefficient

$$r = \frac{k_{zi} - k_{zt}}{k_{zi} + k_{zt}} \tag{4.24}$$

A wave travelling in free space is travelling with the speed of light and has a wave vector $k_0 = \omega/c$. In a medium, the speed v is reduced and the wave vector k is determined by the real and imaginary parts of refractive index in the material, where $k = \omega\tilde{n}/v$.

$$k = k_r + ik_i = k_0(n_r + n_i) \tag{4.25}$$

Since the imaginary part of the refractive index is related to the absorption through the medium, the incoming wave vector k_{zi} only depends on the real part of the refractive index in the first medium

$$k_{zi} = k_0 n_{r1} \tag{4.26}$$

while the transmitted wave vector k_{zt} is affected by the absorption though the medium, and must include both the real and imaginary parts of the complex refractive index $\tilde{n}_2$

$$k_{zt} = k_0(n_{r2} + in_{i2}) = k_0(\tilde{n}_{2)} \tag{4.27}$$

The resulting reflection coefficient will then be

$$r = \frac{k_0 n_{r1} - k_0(n_{r2} - in_{i2})}{k_0 n_{r1} + k_0(n_{r2} + in_{i2})} = \frac{n_{r1} - \tilde{n}_2}{n_{r1} + \tilde{n}_2} \tag{4.28}$$

The reflection from the surface of medium number two is define as $R = |r^2|$, hence

$$R = \frac{(n_{r1} - \tilde{n}_2)^2}{(n_{r1} + \tilde{n}_2)^2} \tag{4.29}$$

Assuming that medium one is air, with refractive index $n_{r1} = 1$, we have

$$R = \frac{(1-\tilde{n}_2)^2}{(1+\tilde{n}_2)^2} \tag{4.30}$$

An expression for the change in reflection, ΔR can be derived by finding the derivative of R with respect to $\tilde{n}_2$

$$\frac{dR}{d\tilde{n}_2} = \frac{-2(1-\tilde{n}_2)}{(1+\tilde{n}_2)^2} - \frac{-2(1-\tilde{n}_2)^2}{(1+\tilde{n}_2)^3} = \frac{2R}{(1-\tilde{n}_2)} - \frac{2R}{(1+\tilde{n}_2)} = \frac{4R}{\tilde{n}_2^2 - 1} \tag{4.31}$$

This gives the expression for $\Delta R/R$

$$\frac{\Delta R}{R} = \frac{4\Delta\tilde{n}_2}{\tilde{n}_2^2 - 1} \tag{4.32}$$

For an incident angle $\theta \neq 0$, the angle can be denoted θ_1 and the angle of the transmitted beam in the medium can be denoted θ_2. For P-polarized light the reflection coefficient in equation 4.28 will then be given as [30]

$$r_p = \frac{n_{r1}cos\theta_2 - \tilde{n}_2 cos\theta_1}{n_{r1}cos\theta_2 + \tilde{n}_2 cos\theta_1} \tag{4.33}$$

The angle θ_2 of the transmitted beam can be found from Snell's law

$$\tilde{n}_1 sin\theta_1 = \tilde{n}_2 sin\theta_2$$

$$sin\theta_2 = \frac{\tilde{n}_1}{\tilde{n}_2} sin\theta_1$$

So the expression for $cos\theta_2$ can be expressed

$$cos\theta_2 = \sqrt{1 - \frac{\tilde{n}_1^2}{\tilde{n}_2^2} sin^2\theta_1} \tag{4.34}$$

The reflection R_p will then be expressed through the angles

$$R_p = \frac{(n_{r1}cos\theta_2 - \tilde{n}_2 cos\theta_1)^2}{(n_{r1}\theta_2 + \tilde{n}_2 cos\theta_1)^2} \tag{4.35}$$

Inserting the $n_{r1} = 1$ and following the same procedure as normal incident, we get an expression for $\Delta R_p/R_p$

$$\frac{\Delta R_p}{R_p} = \frac{4cos\theta_1 cos\theta_2}{\tilde{n}_2^2 cos^2\theta_1 - cos^2\theta_2}\Delta\tilde{n}_2 \tag{4.36}$$

In the same way, the reflection for s-polarized light can be found

$$\frac{\Delta R_s}{R_s} = \frac{4\tilde{n}_2 \cos\theta_1}{(\tilde{n}_2^2 - 1)[\tilde{n}_2^2 - \sin^2\theta_1]^{1/2}}\Delta\tilde{n}_2 \tag{4.37}$$

4.3 Drude model

The reflection is related to the complex refractive index $\tilde{n}$ of the material. This expression can be derived by the Drude model, which describes the free carrier contribution to the refractive index change:

$$\tilde{n} = \sqrt{1 - \left(\frac{\omega_p}{\omega}\right)^2} \tag{4.38}$$

where the plasma frequency ω_p is defined

$$\omega_p^2 = e^2 n_{eq}/(\epsilon_0 m^*) \tag{4.39}$$

and m^* is the effective mass for the material, and n_{eq} is the carrier density in equilibrium. The basic idea is that the plasma of free charged carriers in the semiconductor, reflects light below the plasma frequency ω_p.

For simplicity we define a parameter β as

$$\beta = \frac{e^2}{m^* \varepsilon_r \varepsilon_0 \omega^2} \tag{4.40}$$

This simplifies the expression for the refractive index

$$\tilde{n} = \sqrt{1 - \beta \cdot n} \tag{4.41}$$

To see how the refractive index is changing with respect to the carrier concentration n we perform an expression for the derivative of $\tilde{n}$ with respect to n

$$\frac{d\tilde{n}}{dn} = \frac{1}{2\sqrt{1 - \beta \cdot n}} \cdot (-\beta) = -\frac{\beta}{2\tilde{n}} \tag{4.42}$$

The relative change in refractive index $\Delta\tilde{n}/\tilde{n}$ is then given as

$$\frac{\Delta\tilde{n}}{\tilde{n}} = -\frac{\beta}{2\tilde{n}^2}\Delta n \tag{4.43}$$

where Δn is the change in carrier density $[m^{-3}]$ due to photoexcited electrons. Inserting the expression for β given in equation 4.40 we get the expression

$$\frac{\Delta\tilde{n}}{\tilde{n}} = -\frac{1}{2\tilde{n}^2}\frac{e^2}{m^* \varepsilon_r \varepsilon_0 \omega^2}\Delta n \tag{4.44}$$

The change in refractive index can then be expressed as

$$\Delta\tilde{n} = -\frac{1}{2\tilde{n}}\frac{e^2}{m^* \varepsilon_r \varepsilon_0 \omega^2}\Delta n \tag{4.45}$$

From it can seen that the contribution from free-carrier response will give a negative change in the reflectivity.
As discussed in section 4.1, we will neglect the contribution from the imaginary part of the refractive

index for Silicon for the wavelength range of visible light. This gives a value for the refractive index $\tilde{n} = n_r = \sqrt{\varepsilon_r} = 3.7$. ω is given as $\omega = 2\pi c/\lambda$. For a n-doped Si the effective mass for electrons is $m_n^* = 0.26m_e$, while the hole effective mass is $m_h^* = 0.37m_e$. Hence, the expression can then be calculated for n-doped silicon

$$\Delta n_r = -\frac{1}{2 \cdot (3.7)^3} \frac{(1.6 \times 10^{-19})^2 \cdot (800 \times 10^{-9})^2}{0.26 \cdot 9.1 \times 10^{-31} \cdot 8.85 \times 10^{-12} \cdot (2\pi \cdot 3 \times 10^8)^2} \Delta n \tag{4.46}$$

$$\Delta n_r \approx 2.2 \times 10^{-29} \Delta n \tag{4.47}$$

While for a p-doped Si,

$$\Delta n_r = -\frac{1}{2 \cdot (3.7)^3} \frac{(1.6 \times 10^{-19})^2 \cdot (800 \times 10^{-9})^2}{0.37 \cdot 9.1 \times 10^{-31} \cdot 8.85 \times 10^{-12} \cdot (2\pi \cdot 3 \times 10^8)^2} \Delta p \tag{4.48}$$

$$\Delta n_r \approx 1.53 \times 10^{-29} \Delta p \tag{4.49}$$

For a p-polarized probe beam with an incident angle $\theta_1 = 45\,\text{deg}$, θ_2 can be calculated

$$cos\theta_2 = \sqrt{1 - \frac{sin\theta_1}{n_r^2}} = \sqrt{1 - \frac{sin(45)}{3.7^2}} = 0.974 \tag{4.50}$$

The expression for $\Delta R_p/R_p$ in 4.36 can then be calculated

$$\frac{\Delta R_p}{R_p} = \frac{4cos\theta_1 cos\theta_2}{n_r^2 cos^2\theta_1 - cos^2\theta_2} \Delta n_r = \frac{4cos(45) \cdot 0.974}{(0.37)^2 cos^2(45) - 0.974^2} \Delta n_r \qquad = 0.316 \Delta n_r \tag{4.51}$$

and similar for $\Delta R_s/R_s$ in equation 4.37

$$\frac{\Delta R_s}{R_s} = \frac{4n_r \cos\theta_1}{(n_r^2 - 1)[n_r^2 - \sin^2\theta_1]^{1/2}} \Delta n_r = \frac{4 \cdot 3.7 \cos(45)}{3.7^2 - 1)[3.7^2 - \sin^2(45)]^{1/2}} \Delta n_r \qquad = 0.227 \Delta n_r \tag{4.52}$$

So, a simplified expression for $\Delta R_p/R_p$ can be derived from equation 4.47, 4.49 and 4.51. Hence, for a n-doped material with an excitation density Δn $[m^{-3}]$

$$\frac{\Delta R_p}{R_p} \approx 0.316 \cdot 2.2 \times 10^{-29} \Delta n = 6.95 \times 10^{-30} \Delta n \tag{4.53}$$

and a p-doped material with excitation density Δp $[m^{-3}]$

$$\frac{\Delta R_p}{R_p} \approx 0.316 \cdot 1.53 \times 10^{-29} \Delta p = 4.84 \times 10^{-30} \Delta p \tag{4.54}$$

The same procedure can be done for s-polarized light. For n-doped material

$$\frac{\Delta R_s}{R_s} \approx 0.227 \cdot 2.2 \times 10^{-29} \Delta n = 5 \times 10^{-30} \Delta n \tag{4.55}$$

and for a p-doped material

$$\frac{\Delta R_s}{R_s} \approx 0.227 \cdot 1.53 \times 10^{-29} \Delta p = 3.47 \times 10^{-30} \Delta p \tag{4.56}$$

These value are represented in table 4.1, in terms of $[cm^{-3}]$.

Table 4.1: Delta R/R dependence of the carrier density (n, p) [cm^{-3}] for s- and p-polarized light and for n- and p-doped materials

	P-polarized	**S-polarized**
N-doped	$7.0 \times 10^{-24} \cdot \Delta n$	$5 \times 10^{-24} \cdot \Delta n$
P-doped	$4.8 \times 10^{-24} \cdot \Delta p$	$3.5 \times 10^{-24} \cdot \Delta p$

4.4 Conductivity

The electric current density is proportional to the incoming electric field,

$$J = \sigma E \tag{4.57}$$

The Drude model treats the conduction electrons as independent particles that are free to move between scattering events, and assumes that the behaviour of electrons in a solid can be treated classically. An expression for the frequency-dependent conductivity can then be derived [8, 30]

$$\tilde{\sigma}(\omega) = \frac{\omega\epsilon_0\omega_p^2\tau^2 + i\epsilon_0\omega_p^2\tau}{\omega^2\tau^2 + 1} = \frac{\sigma_{dc}(1 + i\omega\tau)}{\omega^2\tau^2 + 1} \tag{4.58}$$

where τ is the momentum relaxation time, or collision time. σ_{dc} is the optical DC current given in Scholler et al. in reference (article 13)

$$\sigma_{dc} = \epsilon_0\omega_p^2\tau \tag{4.59}$$

where ω_p^2 is the plasma frequency defined in XXX

The electrical conductivity can be expressed by the electron mobility μ,

$$\sigma_{el} = nq\mu$$

and ideally the electrical and optical conductivity equal each other.

$\tilde{\sigma}$ can be expressed through the real part of the conductivity, σ_r and the imaginary part, σ_i, [15, 8]

$$\tilde{\sigma} = \sigma_r + i\sigma_i = 2n_r n_i\epsilon_0\omega + i\epsilon\omega(1 - n_r^2 + n_i^2) \tag{4.60}$$

The mobilities μ of holes and electrons are affected by the frequencies of the scattering events taking place in the valence and the conduction band. Impurity atoms from doping, creates scattering centres which might have an influence on the mobility. At low doping concentrations the scattering processes are determined by the lattice, because the contributions from other scattering centres are negligible. However, at high doping concentrations the impurity atoms contribute significantly to the scattering frequency, and the hole and electron mobilities are reduced. The relation between σ and μ is

$$\sigma = nq\mu_e \tag{4.61}$$

Hence, the mobility is given as

$$\mu_e = \frac{\sigma}{nq} \tag{4.62}$$

4.5 Intraband contribution

The interband contribution occurs as a result of three separate effects: state filling, band-gap renormalization and lattice temperature changes.

The lattice-temperature and state-filling responses vary with the time-dependence of the excited carrier density n and the carrier temperature T_e. Right after the pump pulse excitation, the carrier density will increase and hence contribute to a positive change in reflectivity. As time passes, n will decrease as recombination take place and the contributions will be smaller. Hence, the contributions from state-filling and lattice-temperature response give an increased reflectivity. However, contribution from free carriers described by the Drude model is expected to be the dominated contribution in Si, but as time passes and recombination becomes dominant, the lattice-temperature contribution may be significant in reflectivity variations [29].

Band gap renormalization might also affect changes in reflectivity, but these contributions are hard to measure. For large excitation densities, carrier many-body effects may occur, resulting in a reduced optical bandgap. This is equivalent to a larger photon energy and for Si this will result in a positive change in refractive index n. However, this only occurs for carrier densities above a critical value n_{cr}, and for densities below this, bandgap renormalization is absent. Bennett et al. in reference [6] have found the critical density for Si to be $n_{cr} = 6 \times 10^{18}$.

Chapter 5

Experimental setup

In this chapter the a general introduction to pump-probe technique and setup is given, which included theory about the main setup components. The detailed laser properties for the experiments in this work are then presented. Finally, the experimental techniques in addition to pump-probe measurements used in this theses, are described briefly.

5.1 Basic pump-probe technique

A pump-probe experiment enables us to investigate the relaxation behaviour of excited carriers in a semiconductor, on a picosecond time scale. The way this is done is by sending an ultrashort pulsed laser beam into the sample of interest. The intense pump pulse excites carriers across the band gap, causing a change in the material properties, and brings the sample out of its equilibrium state. The interactions which take place in the material can be measured by sending a second ultrashort pulse towards the sample. This second probe pulse is less powerful and arrives at the sample with a time delay τ relative to the pump pulse. The pump and the probe beams overlap spatially on the sample, with the probe beam completely covered by the pump beam. The reflected probe pulse is measured for a range of time delays. As the carriers in the material evolve towards the initial equilibrium state, a corresponding change can be measured in the reflected probe beam intensity. Hence, important information about the carrier dynamics in the sample can be obtained by analysing the probe reflection change [40, 33, 36].

The reflectivity of the sample is found by measuring the reflected probe pulse. The reflectivity, in %, is denoted R. When the sample is exposed to the pump pulse, the measured change in reflected probe signal is denoted ΔR and is given in Volts. From this the resulting change in reflected probe signal can be calculated as $\Delta R/R$. This value is of great importance because it provides information about the excitation density generated, the absorption coefficient in the material and the change in refractive index caused by the pump excitation.

The experimental setup in this work is shown in figure 5.2. This is a also a general setup for a pump-probe measurement performed in reflection.

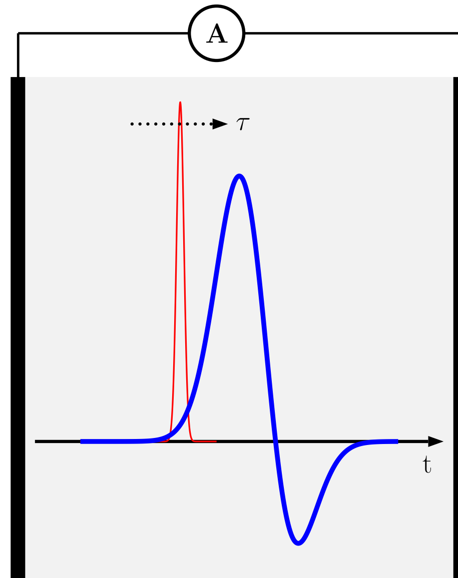

Figure 5.1: Schematic presentation of the pump and probe pulses. The probe pulse has a time delay τ relative to the pump.

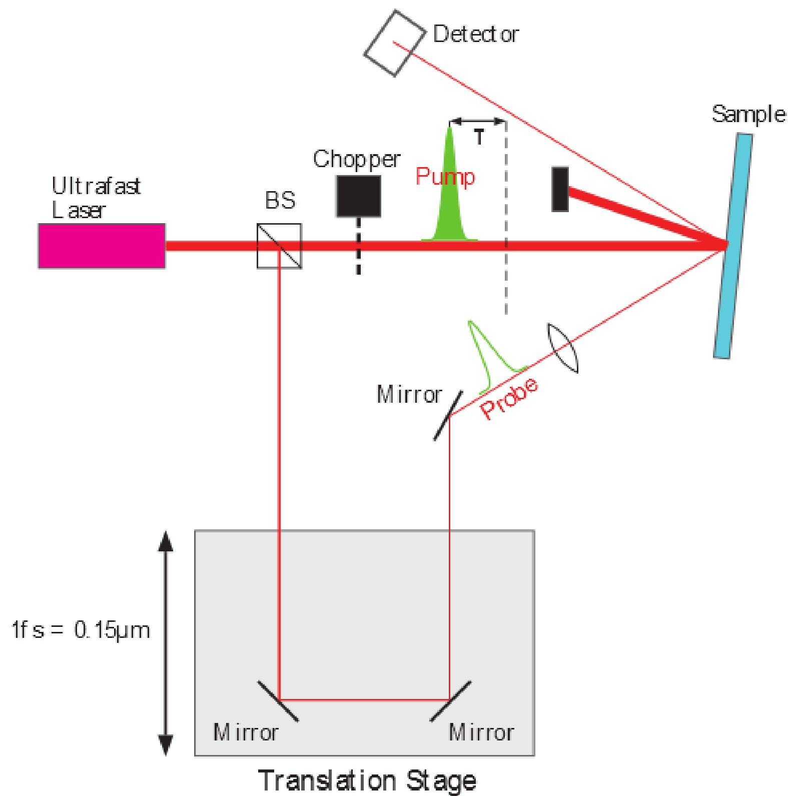

Figure 5.2: Experimental setup for pump-probe measurements detecting the reflected probe signal.

5.2 Lasers

The term *ultrafast lasers* is often used when referring to mode-locked lasers that emit ultrashort pulses. A mode-locked laser is able to generate a train of short optical pulses. Femtosecond lasers are in this category and produces laser pulses with short pulse duration, typically in the time domain of femtoseconds (10^{-15} s).

This is done by keeping the phase relations between a large number of longitudinal modes fixed, or locked, and sustain a simultaneous oscillation among the multiple modes. The interference among the modes will create the short pulses. A typical mode-locked laser consists of a resonator with an intracavity modulator, which modulates the amplitude or the phase of the field inside the cavity. The result is generated short pulses.

A number of modes are allowed in the laser cavity of length L, and usually they oscillate with random phase and irregular amplitudes. This give rise to a time-varying amplitude within the round trip period $T = 2L/c$, where c is the speed of light. However, if the modes have the same phase, they will generate constructive interference at the same time of the round trip, at $T_0 = (\phi/2\pi)T$. Hence, a series of mode-locked laser pulses will be generated at T_0, $T_0 + T$, $T_0 + 2T$... The period T between them is the inverse of the pulse repetition rate f_{rep}. Each pulse containing the phase-locked modes has a small span of frequencies f_0. The width Δt of each pulse is approximately equal to the to the inverse of this span [24, 27].

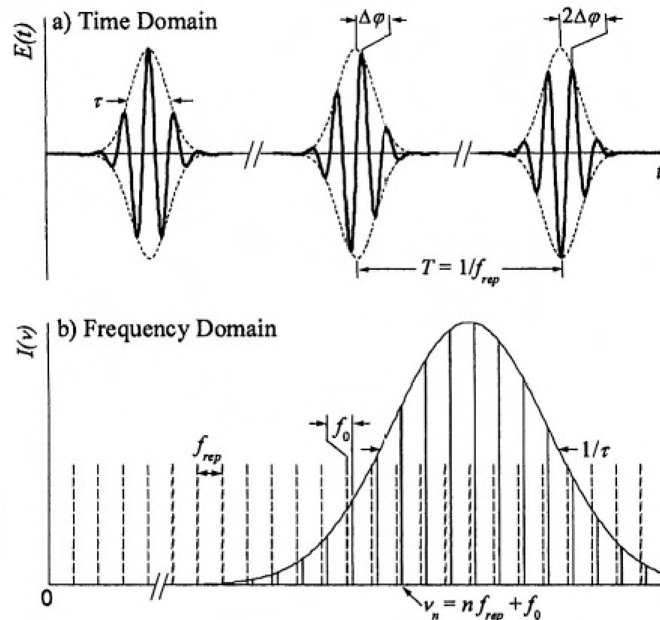

Figure 5.3: Illustration of the concepts behind a mode-locked laser. The upper figure shows the time domain description of a mode-locked laser, with the carrier envelope phase $\Delta\phi$. The lower figure shows the frequency domain description, with a pulse repetition rate f_{rep} and a comb offset due to pulse shifts f_0. Illustration taken from [14].

Mode-locking in time domain is related to a single pulse travelling back and forth between two mirrors, where the loss on the output mirror is compensated by the gain each round trip pumping. The carrier-envelope is based on the decomposition of the pulse into a continuous carrier wave in the time-domain. The carrier-envelope phase, $\Delta\phi$, represents the phase shift between the peak of the envelope and the closest carrier wave peak, or the difference between the group and phase velocities. When $\Delta\phi$ is constant, identical pulses are emitted from the mode-locked laser. Figure 5.3 shows the time- and frequency-domain description for a mode-locked laser.

The benefits achieved in developing ultrafast lasers by mode-locking, are a more accurate phase control and a greater stability. Due to a higher peak power produced from the short pulses, they experience lower loss, which is a great advantage in mode-locked operations [**?**].

The laser system used to perform pump-probe experiments in this report, is a commercial femtosecond Ti:Sapphire amplifier (Solstice, Newport Corporation). A schematic of this system is presented in figure 5.4 and consists of five main parts: a seeding laser (Mai Tai), a pump laser (Empower), a stretcher, a compressor and a regenerative amplifier. In the following, each part will be described briefly. The information is based on the Solstice user manual found in [22].

The Mai Tai consists of two components. The first one is a continouse wave (CW) diode-pumped laser, which produces the ultrafast seed pulses for amplification. The CW has an average output power of 1.1 W and a wavelength of 798 nm. The second component is a mode-locked Ti:Sapphire resonator including a Ti:Sapphire rod, focusing mirrors and other optical devices. The Mai Tai is able to deliver a tunable pulsed power output with repetition rate 80 MHz and with a range of wavelengths from 790 to 810 nm. The CW pump laser is based on the Spectra-Physics *Millenia* diode-pump laser and the mode-locked Ti:Sapphire laser is based on the Spectra-Physics *Tsunami* femtosecond laser.

The next part in the Solstice setup is the Empower pump laser, which is a frequency-doubled diode-pumped ND:YLF laser. It produces a pulsed green beam with wavelength 527 nm which provides the optical energy used to amplify the pulses. The heart of the Empower is a rod of Nd: YLF (lithium yttrium fluoride doped with neodymium). An array of diode lasers pump the Nd:YLF rod, causing it to excite neodymium atoms at wavelength 1053 nm. Through frequency-doubling, the 1053 nm light is coneverted to 527 nm green light and emitted as energetic Q-switched pulses. Q-switching is a technique of concentrating the continuous optical output into series of brief, high-powered pulses. These pulses contribute in the amplification of the mode-locked seed pulses from the Mai Tai.

The high intensities from the laser pulses may cause damage in the amplifier crystal. To prevent this, a grating-based pulse stretcher is used to decrease the peak intensity. The phenomenon called *group velocity dispersion* (GVD) consists of delaying or advancing some wavelengths relative to others. This technique might be shortened to *chirp*, and is used for stretching a very short seed pulse to increase its duration and hence, reduce its peak power. The stretcher chirps the 100 fs transform-limited oscillator pulse and is able to increase the pulse duration by as much as 10^4 times by using dispersive optics to form the pulse stretcher. This is illustrated in figure 5.5, where a short pulse is spectrally spread by making one end of the spread pulse travel faster than the

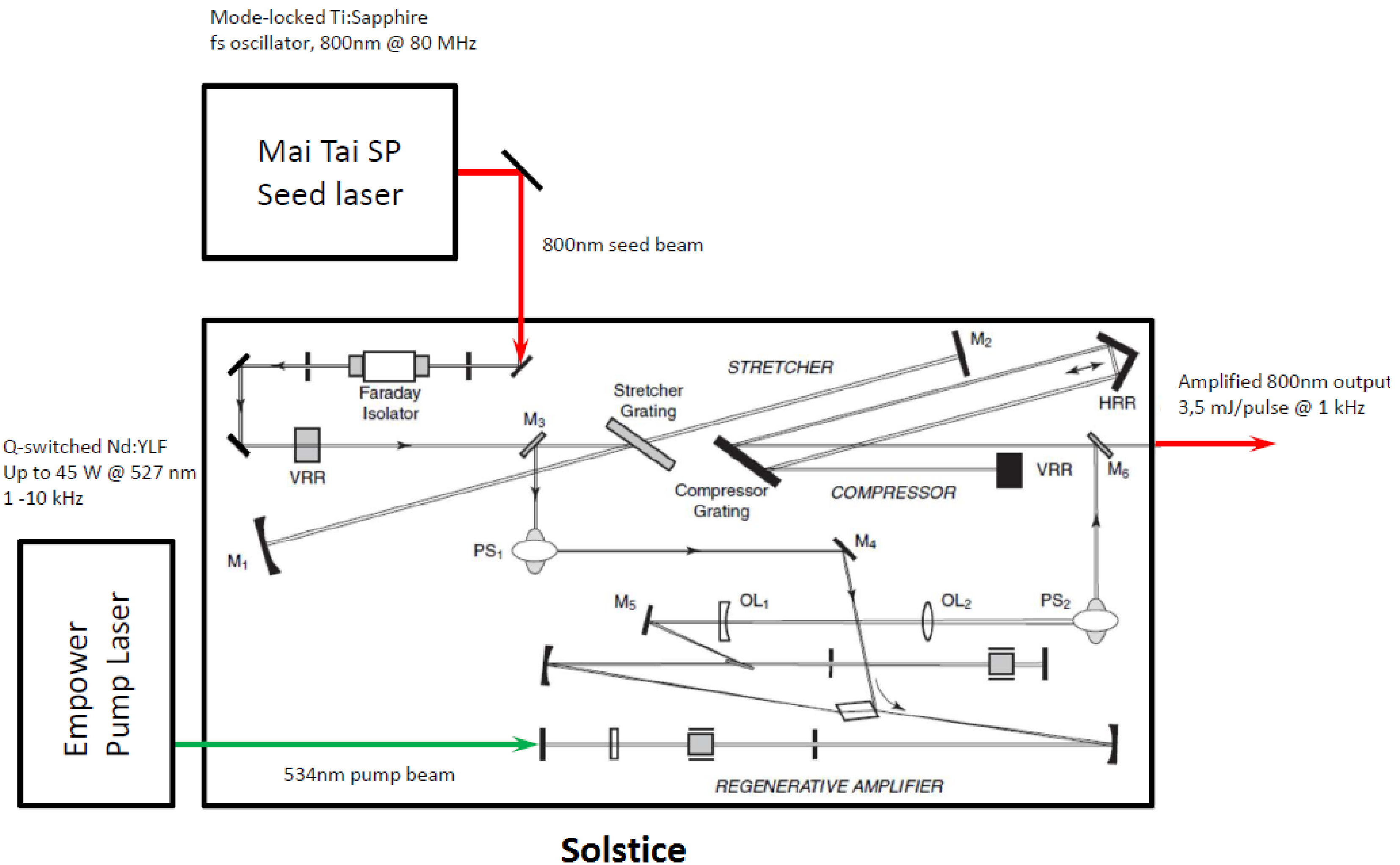

Figure 5.4: Optical layout of the Ti: Sapphire laser Solstice, with Mai Tai SP seed and Empower pump. Illustration provided by the manufacturer.

other. This leads to a temporally broadened pulse. The same principles and optical components are used to compress the laser pulse in the reverse processes, to replicate the high power pulse.

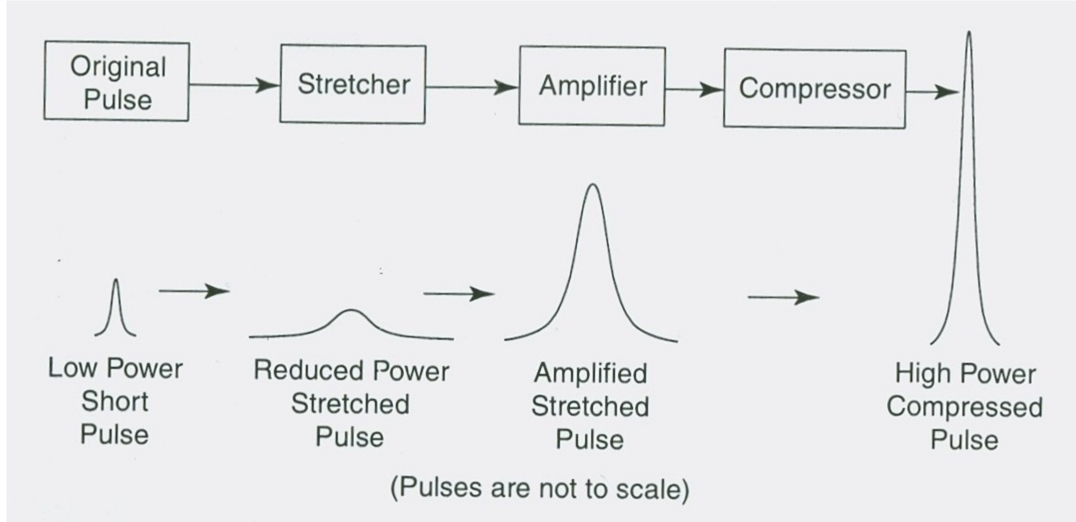

Figure 5.5: Schematics of the pulse stretcher used in the process called chirp. Stretching is important to prevent damage in the amplifier crystal. The reverse process can then be performed to recover the high power pulse.

The pulses generated in the Empower laser play an important role in pumping the Ti:Sapphire regenerative amplifier, which is the fifth main component in the Solstice setup. The pumping repetition rate is 1 kHz and the regenerative amplifier is designed to amplify individual pulses from the mode-locked Ti:Sapphire laser. When the Ti:Sapphire is excited by the pump pulses, it changes into a gain medium for a short period of time. The regenerated amplifier contains synchronized Pockels cells to let in the train of mode-locked seed pulses from the stretcher. As a result, only one stretched pulse can enter the amplifier in a periode of 1 ms. A stretched pulse is synchronezed with the Pockels cell, to let it out after amplification and then in to the compressor.

Finally, the last process is in the Solstice system is the grating-based pulse compressor. The compressor restores the amplified stretched pulse, back to a 100 fs transform-limited pulse. The technique used are called negative chirp. The final output of the laser system used in this work, has a continouse-wave average power of 3.5 W, and an energy of 3.5 mJ/pulse, and wavelength of 800 nm, a diameter of 7 mm and a repetition rate of 1 kHz.

An auto-correlator is an instrument which displays the temporal pulse shape and calculates corrsponding the full-width-half-maximum (FWHM). Figure 6.8 shows the display of an auto-correlator describing the Solstice laser beam used in this work. The calculated FWHM is 130 fs and the laser pulse has a $sech^2$ shape. The corresponding pulse width can be found by multiplying the FWHM value by 0.65. The peak power are related to pulse width and the average pulse power through the equation below.

$$\Delta t_{pulse} = 0.65 \cdot 130\ fs = 85\ fs \tag{5.1}$$

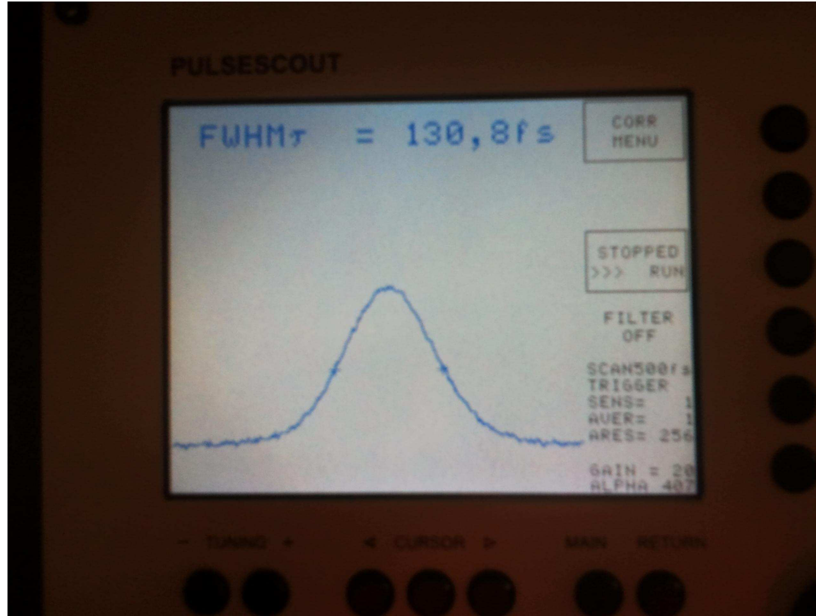

Figure 5.6: The measured signal displayed on the autocorrelator, showing a FWHM of 130 fs. The output power is 3.4 W.

$$P_{av} \cdot \Delta t_{rep} = P_{peak} \cdot \Delta t_{pulse} \tag{5.2}$$

$$P_{peak} = \frac{P_{av} * \Delta t_{rep}}{\Delta t_{pulse}} = \frac{3.6 \times 10^{-3}}{85 \times 10^{-15}} W = 42\ GW \tag{5.3}$$

The pulse wavelength $\lambda = 800$ nm corresponds to a photon energy

$$E_{photon} = h\nu = hc/\lambda = \frac{6.63 \times 10^{-34} \cdot 3 \times 10^{8}}{800 \times 10^{-9}} = 2.49 \times 10^{-19} J = 1.55\ eV \tag{5.4}$$

5.3 Lock-in amplifier

Measuring a small signal in a noisy background is challenging when the amplitude of the noise is much greater than the signal. A lock-in amplifier can extract the signal from noise and give a clear output signal. It can measure the signal of interest down to a few nanovolts even when the noise is thousands of time larger [41, 31, 34].

A lock-in amplifier can measure the voltage V of a sinusoidal signal on this form:

$$V_{in}(t) = V_0 * cos(\omega t) \tag{5.5}$$

The lock-in needs a reference input signal which is synchronized with the input signal we want to measure. With the reference signal the lock-in can measure the signal at the given frequencies and disregard everything else that is not synchronized with the reference signal and outside the region of interest. Appendix A gives a more detailed description of how a lock-in amplifier operates, in

order to measure a small change in the reflected signal.

In this experiment we have used a lock-in amplifer of model SR830 DSP Lock-in Amplifier from Stanford research system with an internal resistivity of 10 MΩ.

5.4 Chopper Frequency

The pump beam is passing a chopper with a define frequency which determines how often the pump arrives at the sample. Figure **??** shows how the chopper frequency limits the number of pump pulses allowed through. The chopper is used on the pump beam to minimize background light and reduce low frequency noise of the probe pulse. This is done by choosing a suitable large chopper frequency so the signal is shifted away from the noise level [40].

However, in the literature there seems to be a confusion over what is the optimum chopper frequency. Zhang's group at Rensselaer Polytechnic advocates a chopper frequency of 125 Hz for a laser with a 1 kHz repetition rate, while the Dutch groups led by Bakker and Woutersen choose a chopper frequency of 500 Hz for the same laser repetition rate. We are not sure why they don't use the pulsed laser at 1 kHz as the reference frequency for the lock-in in the first place, no chopper needed and shorter data acquisition times.

Using Figure 5.7 we will attempt to model the chopped signal using Fourier analysis. An essential

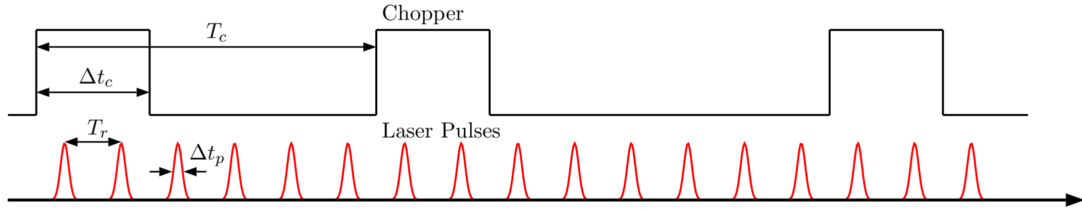

Figure 5.7: Generic timing for chopper.

tool in this analysis is the comb function, $III(t)$, defined as

$$III(t) = \sum_{n=-\infty}^{\infty} \delta(t-n) \tag{5.6}$$

For a pulse train, $p(t)$ with repetition rate T_r we can write it as (ignoring that these are 100fs $sech^2$ pulses and treating them as Dirac delta pulses instead)

$$p(t) = \frac{1}{T_r} III\left(\frac{t}{T_r}\right) \tag{5.7}$$

and it has an accompanying Fourier transform

$$P(\nu) = III(T_r\nu) \tag{5.8}$$

The chopper can be described as a convolution between a rect-function and a comb function, again using Figure 5.7 we obtain

$$chopper(t) = rect\left(\frac{t}{\Delta t_c}\right) * \frac{1}{T_c} III\left(\frac{t}{T_c}\right) = \sum_{n=-\infty}^{\infty} rect\left(\frac{t-nT_c}{\Delta t_c}\right) \tag{5.9}$$

The chopped pulse train, i.e. the signal $s(t)$ seen by the detector, is then mathematically described as

$$s(t) = p(t) \cdot chopper(t) \tag{5.10}$$

This signal, in the frequency domain, will look like

$$S(\nu) = P(\nu) * Chopper(\nu) = \sum_{n=-\infty}^{\infty} \frac{|\Delta t_c|}{T_r} e^{-i2\pi\nu n T_c} \, sinc\left(\Delta t_c \nu - \frac{n\Delta t_c}{T_r}\right) \tag{5.11}$$

From these calculations we can conclude that a chopper frequency $\nu = 1kHz$ should work in the same way as a chopper at $\nu = 125Hz$. Equation 5.11 indicates that a smaller ν might even give a better signal $S(\nu)$.

To improve the experimental setup, the chopper frequency was increased from 125 Hz to 500 Hz. The measurements showed a smoother curve with a larger amount of data points for each scan. Consequently, the chopper frequency was set to 500 Hz for all measurements. The frequency generator used was from Stanford research system and of model SR540 Chopper Controller.

5.5 Laser beam properties

5.5.1 Pump beam

An iris with radius $W_0 = 2.75$ mm is used to reduce the pump area, and the beam is then focused by a lens of focal length $f = 1$ m. The sample is located 0.74 m away from the lens, which means that the distance from the sample to the focal point of the lens is $z = 1 - 0.74 = 0.26$ m. The beam radius in the focal point is denoted $W_0\prime$ and the focused pump beam radius at sample W is given by the equation

$$W = W_0\prime \sqrt{1 + (\frac{z}{z_0})^2} \tag{5.12}$$

where $W_0\prime$ and z_0 are defined as

$$W_0\prime = \frac{\lambda * f}{\pi W_0} \tag{5.13}$$

$$z_0 = \frac{\pi W_0\prime^2}{\lambda} \tag{5.14}$$

The pump radius at the sample can then be calculated as

$$W_0\prime = \frac{800 \times 10^{-9} \cdot 1}{\pi \cdot 2.75 \times 10^{-3}} = 9.26 \times 10^{-5} \; m$$
$$z_0 = \frac{\pi \cdot (9.26 \times 10^{-5})^2}{800 \times 10^{-9}} = 3.37 \times 10^{-2} \; m$$

$$W(z = 0.26) = 9.26 \times 10^{-5} \sqrt{1 + \left(\frac{0.26}{3.37 \times 10^{-2}}\right)^2} = 7.21 \times 10^{-4} m = 721 \; \mu m \tag{5.15}$$

This radius gives a pump beam area

$$A = \pi W(z = 0.26)^2 = \pi \cdot 7.21 \times 10^{-4} = 1.63 \times 10^{-6}\ m^2 = 1.63 \times 10^{-2}\ cm^2 \tag{5.16}$$

The penetration depth in silicon for 800 nm is approximately 10 $\mu m = 10 \times 10^{-4}\ cm$. This means that the effective volume where the pump interacts with the silicon atoms, is

$$V = A \cdot 10\ \mu m = 1.63 \times 10^{-2} \cdot 10 \times 10^{-4}\ cm^3 = 1.63 \times 10^{-5}\ cm^3 \tag{5.17}$$

The incident angle of the pump beam was measured to 5° from the sample's normal, with an estimated measured error of ±1°.

The pump beam power is reduced after passing the chopper and the iris. The average pump power at the sample was measured to P_{av} = 100 mW with an estimated measured error of ±5 mW. This gives the average pump intensity

$$I_{av} = \frac{P_{av}}{A} = \frac{0.1}{1.63 \times 10^{-2}}\ W/cm^2 = (6.14 \pm 0.31)\ W/cm^2 \tag{5.18}$$

The pump peak power is then given by

$$P_{peak} = \frac{P_{av}\Delta t_{rep}}{\Delta t_{pulse}} = \frac{0.1 \cdot 1 \times 10^{-3}}{85 \times 10^{-15}} = 1.18\ GW \tag{5.19}$$

The pump fluence is defined as energy in one laser pulse per area. This tells us how much energy the sample is exposed to for each pump pulse. For our setup, the laser repetition rate is 1 kHz which gives 1000 pulses per second. This gives an energy

$$0.1\ W \rightarrow 0.1\ J/s \rightarrow 0.1 \cdot 10^{-3}\ J/pulse = 100 \pm 5\ \mu J/pulse \tag{5.20}$$

The fluence can then be found, as the energy per area,

$$fluence = \frac{100\ \mu J}{1.63 \times 10^{-2}\ cm^2} = (6135 \pm 300)\ \mu J/cm^2 \tag{5.21}$$

Background research

Compared to other pump-probe experiments of Si in the literature, this fluence is relate hight. In Sabbat et al. work (in reference [24]) a fluence of 2400 $\mu J/cm^2$ was used to generate an excitation density of $5.5 \times 10^{18}\ cm^{-3}$ and a $\Delta R/R \sim 7 \times 10^{-6}$. However, in work of Grischkowsky et al. (in reference [10]), a significant smaller fluence of 0.1 mJ/cm^2 was used, and the resulting $\Delta R/R \sim 2 \times 10^{-6}$, giving rise to an excitation density of $\sim 1 \times 10^{17}\ cm^{-3}$.

For the best signal to-to-noise ration, we initially chose a fluence in the order of 2000 $\mu J/cm^2$, which was right below to the value used in Sabbat et el. measurements. However, when we proceeded on to pump-probe measurements of mc-Si, achieving a good results was more challenging than for single c-Si, and by increasing the pump fluence we experienced a better result and an improved signal-to-noise ratio. Hence, the final fluence we used in all measurements described in this report was chosen in order to improve the signal-to-noise ratio for mc-Si samples.

5.5.2 Number of photons

The number of photons in the pump pulse presents the maximum number of photons that can interact with the atoms in the sample. The rate between the number of excited electrons and number of phonon in the pump pulse is of great interest as it may provides information about sensitivity of the sample, described by the quantum efficiency.

The number of photons in the pump pulse can be found from the energy relation

$$E = Nh\omega = P_{peak}\Delta t_{pulse} \tag{5.22}$$

This gives

$$N = \frac{P_{peak}\Delta t_{pulse}\lambda}{hc} = \frac{1.18\times10^{9}\cdot 85\times10^{-15}\cdot 800\times10^{-9}}{6.6\times10^{-34}\cdot 3\times10^{8}} = 4\times10^{14}\ photons \tag{5.23}$$

5.5.3 Probe beam

A beam sampler is used to extract 1 % of the pump beam to create a probe beam. The area of the probe beam is reduced by an iris with radius $W_0 = 1.5$ mm, and then focused by a lens of focal length $f = 1$ m. The probe radius at the sample can be calculated from equation 5.12-5.14. This gives $W_0\prime = 3.4\times10^{-4}$ m and $z_0 = 0.45$ m. This gives the resulting probe radius at the sample,

$$W_{probe} = 0.45\ mm = 450\ \mu m$$

. The corresponding probe area is

$$A_{probe} = \pi W_{probe}^2 = \pi\cdot 0.45\times10^{-3} = 6.4\times10^{-7}\ m^2 = 6.4\times10^{-3}\ cm^2$$

Probe incident angle is measured to $\theta_1 = 45\,\text{deg}$ relative to the normal of the surface, with an estimated error of $\pm1°$.

Comparing the probe area with the pump area in 5.16, we see that the probe area covers $6.4\times10^{-3}/1.63\times10^{-2} = 39\%$ of the pump area when they overlap at the sample.

The initial probe power was 350 μW before it was reduced by a neutral density filter (ND-filter). The reflected probe signal from the sample surface was measured by a silicon PIN detector from Newport and a phosphor oscilloscope, Tektronix DPO 2014, with a internal resistance 100 MΩ. For each measurement the ND-filter was adjusted such that the reflected signal was 220 mV in the oscilloscope.

5.5.4 Beam polarizations

The pump beam is horizontal polarized. For the (100) and (111) crystal wafers, this corresponds to a pump polarization parallel to the <110> direction in the crystal. The probe beam polarization is either parallel to the pump polarization, along the <110> direction, or perpendicular to the pump

polarization. For the (100) wafers, a perpendicular probe beam corresponds to a polarization parallel to the $<\bar{1}10$ direction in the crystal. While for the (111) wafer, this corresponds to a probe beam polarization along the $<22\bar{1}>$ direction. The perpendicular probe polarization is created by rotating the probe polarization 90° relative to the pump polarization, using a $\lambda/4$ waveplate. The purpose is to investigate the contribution from coherent artifacts and how this affected the measurements. To limit the scattered pump light reaching the detector, a polarizer is included in the setup, which only allows the probe beam polarization through to the detector. An illustration of the experimental setup with perpendicular probe polarization is shown in figure 5.8.

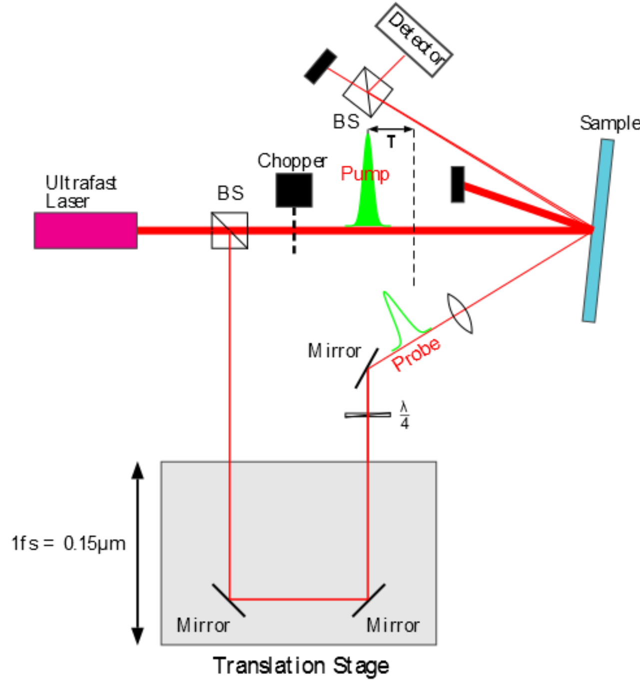

Figure 5.8: Experimental setup for orthogonal pump and probe polarizations. A waveplate is used to rotate the probe polarization perpendicular to the pump polarization, and a polarizer limits the scattered pump light into the detector.

5.6 Experimental preparation

For thick samples L and large absorption α such that $\alpha \cdot L >> 1$, transmission measurements might be hard to achieve. The absorption in Silicon at 800 nm is $\alpha \approx 1 \times 10^5$ [26]. The samples used in this work were mainly in the range of 450 – 530 μm (see table 5.1), which gives $\alpha \cdot L = 1 \times 10^5 \cdot 450 \times 10^{-6} = 45$. For this reason the all the experiments are carried out by measuring the reflection from the samples.

The lock-in amplifier is prepared by using the chopped pump signal as a reference signal, and from this the lock-in produced a reference angle that is used as baseline for the measurements (see section 5.3 and Appendix A). The procedure of resetting the lock-in amplifier to set a new

Table 5.1: Table of silicon samples used in the experiment. Showing the properties: type of doping, crystal orientation, wafer thickness and resistivity.

Category	**Sample number**	**Wafer tag**	**Doping**	**Crystal orientation**	**Thickness [μm]**	**Resistivity [Ωcm]**
Bare c-Si						
	1	bp0	p-doped	(100)	520	0-100
	2	bn0	n-doped	(100)	460	4-7
Repolished	3	rep0	p-doped	(100)	460	0-100
HF-etched	4	hfn0	n-doped	(100)	468	10-20
Passivated						
Nitride	5	nitp0	p-doped	(100)	530	10-20
Oxidized	6	oxp0	p-doped	(100)	460	
Oxidized	7	ox1	unknown	(111)	460	
Oxidized	8	oxn0	n-doped	(100)	470	10-20
Bare mc-Si						
	9	mc1	p-doped	-	250	1
	10	mc2	p-doped	-	120	N/A
	11	mc3	?	-	800	N/A
	12	mc4	?	-	800	N/A

reference angle, is done for each sample or when the setup is slightly changed.

The lock-in amplifier settings Sensitivity and Integration Time may used in a large range of combinations to find the best suitable settings. The best result for our setup is found for a sensitivity of 5 mV together with an integration time of 3 seconds. All the measurements described in this theses are carried out with these settings on the lock-in amplifier.

The step size on the translation stage is set to l = 0.01 m. Through the relation, $t = \frac{2*l}{c}$, this corresponds to t = 66.7 femtoseconds delay time for each step.

5.7 Samples

Three categories of Silicon samples are used in this work: bare single c-Si, passivated single c-Si and bare mc-Si. The information about the material properties of the each sample is not complete. This work will not focus on the detailed background history for each sample, but rather give an overall picture based few known properties. Table 5.1 shows the samples used in this experiment and presents the corresponding known wafer properties.

In order to achieve good pump-probe measurements, this requires only polished samples. This is to insure a good reflection from the sample's surface. In the case of unpolished wafers, too much pump light is scattered at the surface and reaching the detector.

5.8 Probe reflection in equilibrium

The probe reflectivity R for incident angle 45° is measured for parallel and perpendicular polarized probe beams, see table 5.2. These measurements are performed without the pump excitation and with the material in equilibrium. This will be used in the calculation for $\Delta R/R$.

Table 5.2: Measured probe reflection in % from each sample, with probe polarization parallel and perpendicular to the pump polarization. Incident angle is 45°.

Category	**Sample**	**Probe polarization**	
		parallel	**perpendicular**
Bare c-Si			
	bp0	19%	38%
	bn0	20%	38%
Repolished	rep0	20%	38%
HF-etched	hfn0	18%	37%
Passivated c-Si			
Nitride	nitp0	11%	22%
Oxidized	oxp0	16%	31%
Oxidized	ox1	13%	16%
Oxidized	oxn0	18%	35%
Bare mc-Si			
	mc1	20	38%
	mc2	20	38%
	mc3	20	38%
	mc4	20	38%

5.9 Crystal orientations

A (100) wafer has a surface normal in the direction <100>. A horizontal polarized pump light will be parallel to the <110> direction in the crystal. This is illustrated in figure 5.9.

By rotating the crystal around its azimuth, the crystal direction parallel to the pump may change and contribute to a different carrier distribution.
To investigate this contribution to our measurement, all wafers are rotated 90° around its azimuth. The purpose is to look for any noticeable changes since the crystal direction parallel to the pump may change and contribute to a different carrier distribution. Rotating the sample 90° around its azimuth is equivalent to rotating the pump polarization 90°, to vertical direction, while the sample remains in the same position.

For the (100) crystal wafers, see figure 5.9, a rotation by 90° will put the pump polarization along an orientation also described by the <110> direction. Hence, the crystal direction is not changed and we would not expect to see any change in the measurements as a result of rotating (100) wafers. For the (111) crystal sample (wafer ox1 in table 5.1), a 90° rotation of the sample will change the

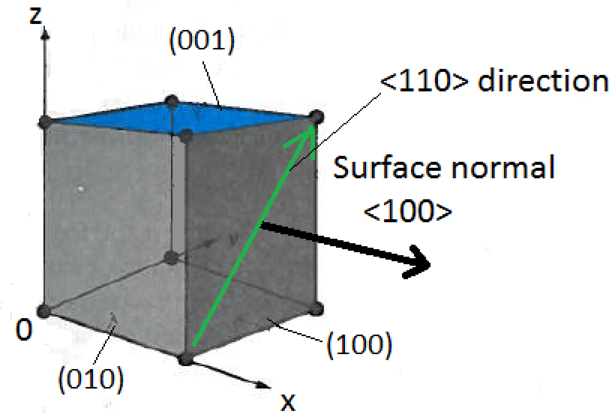

Figure 5.9: Illustration of a cubic crystal structure. A (100) wafer has a normal <100> perpendicular to the <110> directions.

crystal direction parallel to the pump polarization from <110> to <22$\bar{1}$>. This change may result in a slightly different result, which may be observed by pump-probe measurements. The rotation measurements were performed with the probe polarization parallel to the pump polarization.

5.10 Other experimental techniques

Different experimental methods are used in this work, and the techniques will be described briefly in the following.

5.10.1 EBSD mapping

Electron Backscatter Diffraction (EBSD) is a technique used to investigate the crystallographic nature of materials. Any single crystalline or multicrystalline material can be examined. EBSD can provide information about grain size, crystal orientation of grains, grain boundaries character and texture.

The concept behind EBSD is based on a Scanning Electron Microscope (SEM) with an additional phosphor screen, a focusing lens and a camera. The sample is tilted 70 degrees from the incident electron beam in the SEM caber. When the beam hits the sample surface and interacts with the crystal lattice, electron diffraction occurs due to spacing between the crystal planes. Backscattered electrons in the material creates diffraction from different paths, resulting in constructive and destructive interference with the primary beam. The phosphor screen is located along the pathway of the diffracted electrons, and electrons in constructive interference may collide with the phosphorus screen, causing it to florescence. A diffraction pattern can now be observed on the screen. The lens is focusing the image from the phosphor screen onto a camera and the crystalline structure of the sample can be determined [39].

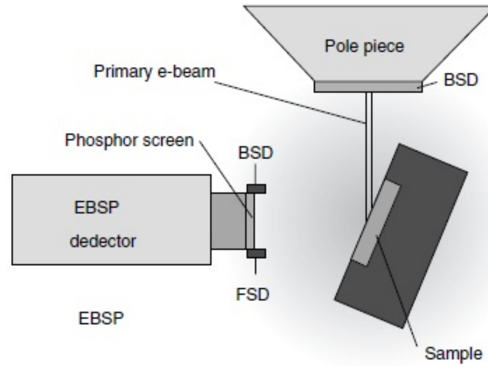

Figure 5.10: A schematic arrangement of a EBSD setup. Illustration taken from [39].

5.10.2 THz-TDS

In this work, THz-TDS measurements will be applied and analysed. The basic concepts behind these measurements are briefly describes below. For further information, see Nuss and Orenstein's paper in reference [23].

Terahertz (THz) pulses are pulses of wavelength from 0.1 mm to 1 mm, thus with frequencies in the terahertz range of $0.3 - 3 \times 10^{-12}$ Hz. One of the great features of THz, is that it can easily penetrate a number of materials. THz radiation can be generated in a number of ways. In this experiment, an ultrashort laser with hight intensity is sent trough a crystal. Due to non-linear effects taking place as the laser pulse propagates though the crystal, the electrical polarization of the crystal is changed and a THz pulse is generated.

Terahertz Time-Domain Spectroscopy (THz-TDS) is a technique where the materials properties are probed with terahertz radiation. As THz radiation is passing through the sample, amplitude and phase are slightly changed after penetrating the material, and the measured transmitted signal can proved information about both amplitude and phase changes over a range of frequencies. To detection the THz signal, a detection beam is also required. This beam is from the same laser beam that generated the THZ pulse and it has to arrive at the same time as the THz pulse in the detector. An electrical signal is produced in the detector depending on whether the electric field of the THz is high or low when the detection pulse arrives. This can be controlled by delaying the detection pulse with a translation stage before it arrives in the detector.

One of the main advantages of Tz-TDS is that the frequency dependent absorption coefficient and index of refraction can be obtained from the detected signal. From this the complex dielectric constant $\hat{\epsilon}$ and complex conductivity $\hat{\sigma}$ can be determined. Hence, Tz-TDS can provide valuable information about the material properties for a wide range of applications.

5.10.3 Microwave Photoconductive Decay

Microwave Photoconductive Decay (MW-PCD) is a nondestructive and noncontact technique used to measure the minority carrier lifetime in semiconductor materials, both as thin films and in the bulk material.

The MW-PCD technique generates excess carriers within the wafer by a short light pulse, which increases the wafer conductance. After termination of the light pulse, the excess carriers recombine and the conductance decays to its initial value. The conductance decay is measured by the reflection of microwaves, as the light pulse leads to a change in the reflected microwave power. Then, the effective carrier lifetime τ_{eff} can be determined by fitting the exponential decay of the measured transient [11].

5.10.4 Reflectivity measurements

Spectral reflectivity measurements is done by using a light source of white light at approximately 90 degrees incident angle. A reflectance probe is used to detect the reflected signal from the sample, which send it to an Avantis Spectrometer. Figure 5.11 shows a schematic presentation of the setup. The reflectance probe contains 7 fibres which are 600 μm in diameter.

Before measurements are performed, some parameter must be calibrated. First a reference level which represents 100 % reflection is set. For this an aluminium mirror is used as to generate a reference signal I_{mirror}. The detected reflection from the sample is measured with this reference signal as a baseline. Black noise is removed by subtracting the background signal without any sample from the measurements. Hence, the reflected signal is measured in the following way

$$I_{reflection} = \frac{I_{signal}}{I_{mirror}} - I_{background} \tag{5.24}$$

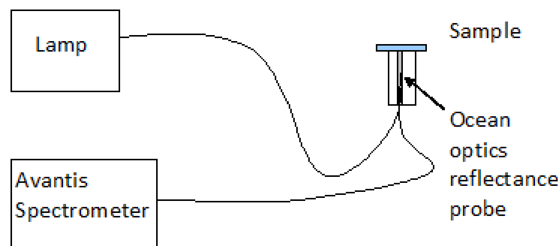

Figure 5.11: A schematic arrangement of spectral reflectivity measurement. A white light source sends light towards the sample and the reflected signal is detected by fibres in the reflection probe.

Chapter 6

Results and discussion

In this chapter the main results will be presented, and the relevant discussion will be made. The total amount of experimental results is large and only the main results will be presented through figures and tables in this chapter.

6.1 Pump reflection

The reflection from the pump beam was measured for each sample, and the results are presented in table 6.1. Comparing the bare and the passivated wafers, the samples nitp0 and oxn0 have a significant lower reflection loss compared to the non-passivated wafers. This is discussed in details in section 6.3.5. Since the reflection loss was smaller, we expected the passivated wafers to generate a larger excitation density in the material.

6.2 Bare single crystalline Si

The first pump-probe measurements were performed on bare single crystalline Si wafers. The goal was to establish a good experimental pump-probe technique and obtain information about carrier dynamics in c-Si, before proceeding to more challenging samples, such as mulitictystalline Si.

The first two measurements were performed on bare n- and p-doped single c-Si. The measurements were carried out with the probe beam parallel and perpendicular to the pump polarization. The detected probe reflections, represented by $\Delta R/R$, are shown in figure 6.1 for the n-doped and p-doped Si. The first observation is a clear change in the reflected signal when to the pump hits the samples and generates a large carrier excitation density. The pump excitation is causing a reduction in the reflected signal, which represent a negative contribution from the Drude free-carrier effect. The lowered signal remains at this level for a longer time than the probe delay time used in these measurements. This corresponds to an excitation density and a free carrier contribution

Table 6.1: Measured pump reflection in % from each sample. Incident angle is 5° and the pump beam polarisation is horizontal.

Category	**Sample**	**Pump reflection**
Bare c-Si		
	bp0	32%
	bn0	32%
Repolished	rep0	31%
HF-etched	hfn0	32%
Passivated c-Si		
Nitride	nitp0	22%
Oxidized	oxp0	31%
Oxidized	ox1	30%
Oxidized	oxn0	9%

which remain constant for a time longer than 20 ps, and no relaxation of carriers can be observed.

In the literature, the carrier lifetime in crystalline Si are found in the range from microseconds to millisecond [21, 24, 29, 42]. A lifetime of 1 μs would require a variable delay line of length $10^{-6} \cot 3 \times 10^8/2 = 150\ m$ in order to measure the entire relaxation process of carriers in silicon. The translation stage used in our experiment is 0.08 m long, and can create time delays up to a maximum of 0.5 nanoseconds. This indicates that carrier lifetimes in crystalline silicon are above the range of possible time delays in a general pump-probe experiment.

Comparing the results in figure 6.1, for parallel and perpendicular probe beams, coherent artifacts are certainly reduced for measurements performed with orthogonal pump and probe polarizations. However, the measured $\Delta R/R$ does also appear smaller. Since the pump is polarized along the same crystal direction <110> in the crystal, we wouldn't expect the number of generate carriers to change. However, the reflection from s-polarized and p-polarized light is different, and since the reflected probe signals in this work were kept constant by adjusting the input probe power, a weaker probe beam was required for perpendicular polarization. Hence, we propose that the slightly changed experimental setup and weaker probe beam might give rise to a lower $\Delta R/R$. However, the slightly different probe powers used in this work should not effect the measurements significantly, since the probe powers are within the linear regime and many orders of magnitude smaller than the pump power.

For simplicity, in the following section only the figures from parallel probe and pump polarization are presented, so the pump and probe polarizations along the <110> direction in the crystal. However, the measured $\Delta R/R$ values for probe polarization along the $<\bar{1}10>$ direction, for all the bare and passivated c-Si samples, are presented in table 6.2. The corresponding excitation densities may be calculated through the equations X, for p- and n-doped Si. The excitation densities are calculated for parallel pump and probe polarizations, and they are also presented in figure 6.2.

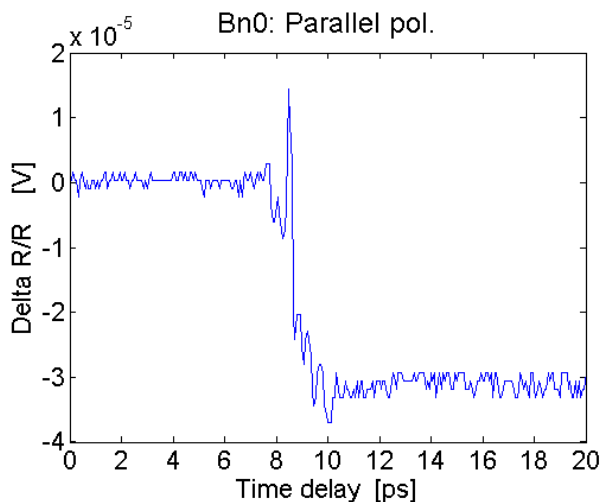

(a) Bn0 parallel polarization

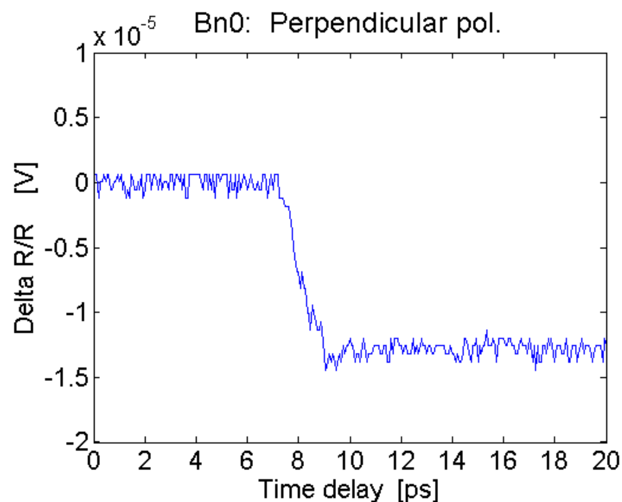

(b) Bn0 perpendicular polarization

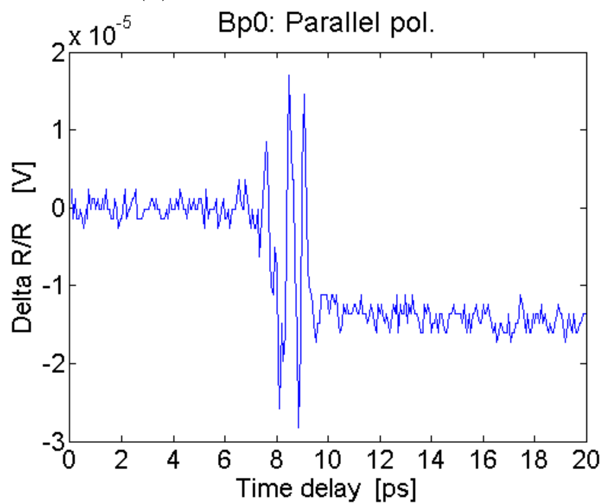

(c) Bp0 parallel polarization

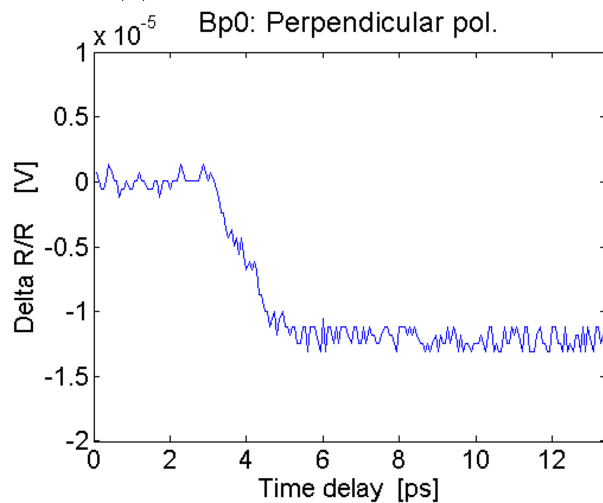

(d) Bn0 perpendicular polarization

Figure 6.1: Pump-probe measurement of the bare samples bn0 and bp0

Table 6.2: Measured $\Delta R/R$ and calculated excitation density for pump-probe measurements on bare and passivated single crystalline Si wafers. The table presents the crystal plane parallel to the pump beam polarization and the probe polarization relative to the pump. The excitation density is calculated for parallel pump and probe polarizations.

Category	**Wafer**	**Pump along crystal direction**	**Δ R / R ×10^{-6}** [V] Probe parallel	Probe perpendicular	**Excitation density** [**cm^{-3}**]
Bare					
	bp0	< 110 >	32	13	4.5×10^{18}
	bn0	< 110 >	14	12	2.9×10^{18}
Repolished	rep0	< 110 >	41	13	8.5×10^{18}
HF-etched	hfn0	< 110 >	37	9	5.3×10^{18}
Passivated					
Nitride	nitp0	< 110 >	155	20	32×10^{18}
Oxidized	oxp0	< 110 >	58	23	12×10^{18}
Oxidized	ox1	< 110 >	171	87	24×10^{18}
Oxidized	oxn0	< 110 >	47	20	6.7×10^{18}

6.3 Passivated single c-Si

6.3.1 Pump-probe results

Pump-probe measurements of the passivated single c-Si wafers, were performed in the same way as for bare c-Si samples. The results from nitp0, oxp0, ox1 and oxn0 wafers can be seen in figure 6.2. From the results we can see that a negative reflection change is produced and it remains at this lower level throughout the delay time. Hence, the results for passivated wafers are in agreement with the observations we did for non-passivated samples. Since the negative contributions from dangling bonds are reduced in the passivated wafers (see chapter 3), this gives us some assurance that the results we obtained for bare Si samples were not dominated by surface states.

From table 6.2 it may be noticed that larger $\Delta R/R$ were measured for the passivated samples, in the range $(47 - 171) \times 10^{-6}\ V$ versus $(14 - 32) \times 10^{-6}\ V$ for bare c-Si. This supports our suggestion, that a lower reflection loss will give rise to a higher excitation density and increase the $\Delta R/R$.

The excitation densities for some of the passivated wafer are above the critical carrier density defined in Chapter 4, $n_{cr} = 6 \times 10^{18}$. This means that bandgap renormalization might contribute to the $\Delta R/R$. However, the results show a negative contribution which indicates that free carriers described by the Drude model dominates.

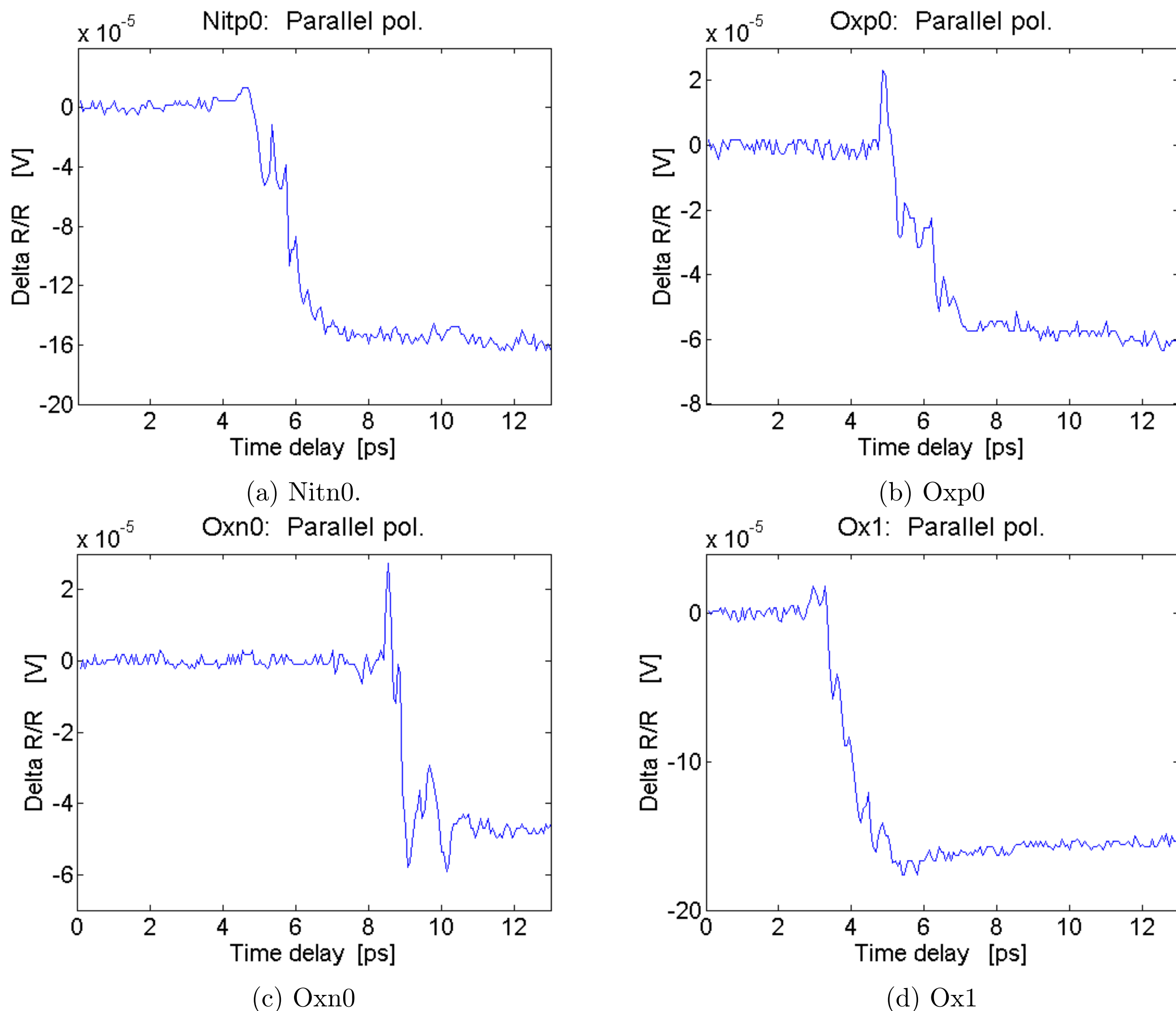

(a) Nitn0.

(b) Oxp0

(c) Oxn0

(d) Ox1

Figure 6.2: Pump probe measurements of the passivated wafers. The pump polarization is along the <110> direction and the probe polarization is parallel to the pump.

6.3.2 Microwave lifetime measurement

The high pump beam fluence used in our measurement might have affected the material properties negatively, by inducing permanent defect at the surface after long time exposure of the pump beam. Microwave lifetime measurement of the oxidized n-doped wafer, oxn0, was performed at IFE in Oslo, aiming to study possible consequences of the high fluence. The main goal was to investigate any spatial differences in the carrier lifetimes over the areas exposed by the pump beam. For details about Microwave Photoconductive Decay (MW-PCD) technique, see Chapter 5.

The lifetime map of wafer oxn0 can be see in figure 6.3. The result shows a spacial lifetime distribution across the wafer. The areas exposed by the pump beam are marked with circles. These circles are within the regions represented by yellow color, corresponding to lifetime of approximately 3 μs. The carrier lifetime in the marked areas are in reasonable agreement with the already spatial distribution of carrier lifetimes. This gives some assurance that we have not created significant damage using the intense pump beam, which is an important indication for our results and for further work.

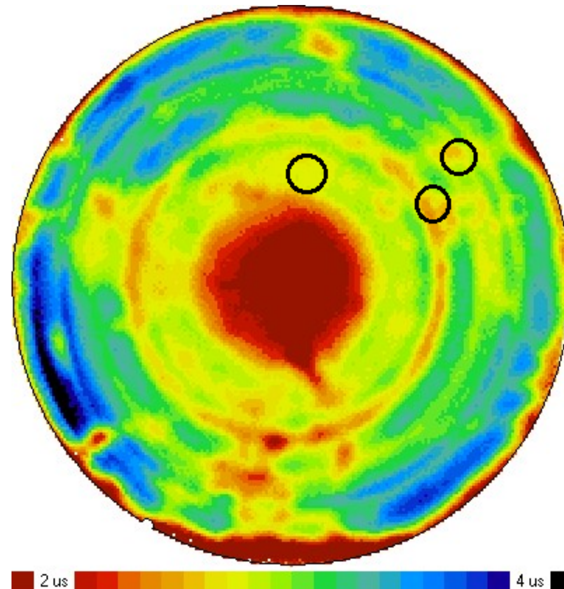

Figure 6.3: Microwave lifetime map of the oxidized n-doped Si wafer. The circles present the areas exposed to the pump beam. The average carrier lifetime across the wafer is found to 2.8 μs.

Figure 6.3 also shows an average carrier lifetime of 2.9μs in the passivated silicon wafer. This confirms our expectations of a carrier lifetime in Si on the time scale of microseconds. Hence, our pump-probe setup was not capable of measuring the average carrier lifetime in silicon.

6.3.3 Passivation thickness

To verify the passivation thickness of the wafers given by the manifacturer, reflection measurements were performed with a light source at approximately normal incident. This gave us the spectral

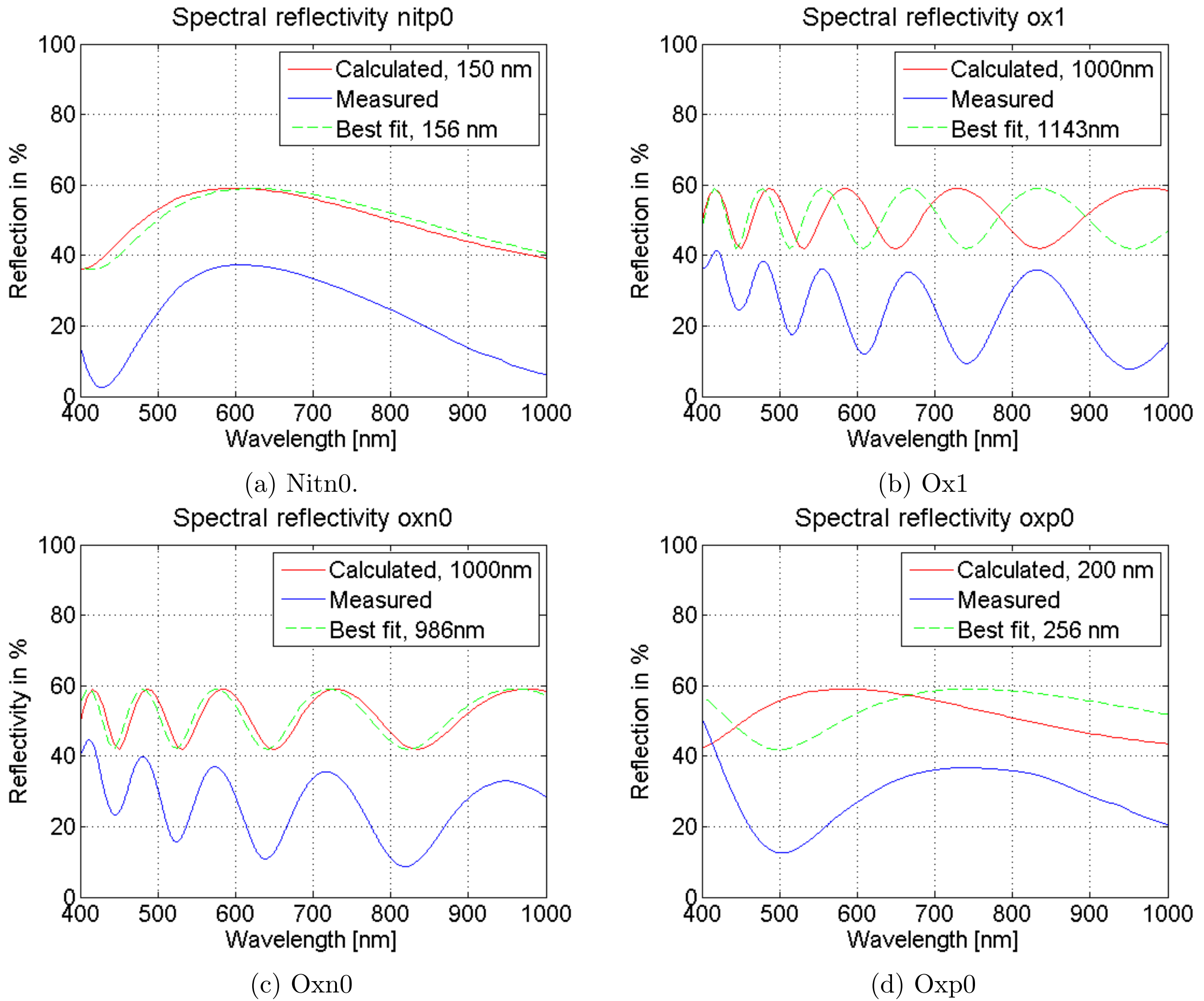

(a) Nitn0. (b) Ox1

(c) Oxn0 (d) Oxp0

Figure 6.4: Presents the spectral reflectivity: found from measurements, calculated with the thickness given by the manufacturer and calculated with an adjusted thickness for a better fit to the measured result.

reflectivity of the passivated wafer over range of wavelength. Details about the setup can be found in Chapter 5.

The reflectivity spectra could also be calculated theoretically, based on the algorithms presented in Abdulahim's paper in reference [4]. Comparing the measured reflectivity spectra, and the theoretical calculated spectra with the specified passivation thickness, we could obtain information about the actual thickness of the passivated layer. This was done by adjusting the theoretical value of the passivation thickness to fit the curvature of the experimental result. The given and the adjusted passivated layer thicknesses are presented in table 6.3, showing the error in the thickness given by the manufacturer.

The adjusted passivation thicknesses are in reasonable agreement with the specified thicknesses

Table 6.3: Presents the passivated layer thickness given by the manufacturer and the adjusted thickness to fit experimental results. The error in the value given the manufacturer is shown.

Wafer	**Thickness of passivation layer**		**Error**
	Given by manufacturer	Best fit to experimental results	
nitp0	150 nm	156 nm	±4%
oxp0	200 nm	256 nm	±2.8%
ox1	1000 nm	1143 nm	±14%
oxn0	1000 nm	986 nm	±1.4%

given by the manufacturer, and within an interval ±1.4 – 14% of the given thickness stated by producers.

From figure 6.4, it can be noticed that the experimental reflected signal is significantly lower than the theoretical signal with the adjusted passivation thickness, for all wavelength. One explanation to this might be that the aluminium mirror used as a reference to 100% reflection, was not a perfect reference. The mirror might contain a coating which increases the reflectivity from the mirror, and giving rise to a lowered measured signal for the samples. In addition, the angle of incident is set to 90° in the theoretical calculations, but in the experimental setup the angle might be a few degrees off 90° incident. This might contribute to a slightly reduced reflected signal and hence, lowering the experimental results.

The reflectance probe in the setup contained 7 fibers in a radius of 3 μm. The distance from the wafer to the fiber was 0.3 mm, which gives an angle of $cos(3\ \mu m/0.3\ mm) = 5.73°$. A certainty estimation may then be found from $cos(5.73))/cos(0) = 0.995$, hence an error of $1 - 0.995 = 5\%$ in the measured reflection due to an small angle off normal incident. This will contribute to lowered measured signal for all samples.

Table 6.4 present the calculated and the measured reflectivity for 800 nm. The possible sources of error discussed above would lead to constant difference between the measured and calculated reflectivity. From the table, we can see a constant difference (33 % less reflection) for all samples but the oxidized p-doped wafer (22 % less reflection). Since we would expect the same error in reflection for all samples, this might indicate that our adjusted passivation thickness for oxp0, was not perfectly accurate and gave a smaller change between the calculated and measured reflectivity for 800 nm.

To support the spectral reflectivity measurements, the pump beam of 800 nm and 5° incident angle was used to measure the reflected signal from the passivated wafers. The measured pump reflectivity for each wafer was slightly below the measured spectral reflectivity for 800 nm, with 2-5 % less reflection. This might be due to small difference in the incident angles.

Table 6.4: Spectral reflectivity for 800 nm light, with the calculated and measured values.

Sample	Calculated	Measured	Difference
nitp0	58 %	25%	33%
ox1	66 %	33 %	33 %
oxn0	44 %	11 %	33 %
oxp0	58 %	36 %	22 %

6.3.4 Removing passivation layer

To examine the effects of passivation on $\Delta R/R$ and the excitation density, the oxidized layer on wafer oxn0 was removed by HF-etching. This took place in Nanolab at NTNU, and the HF-solution was prepared in the manner to remove all of the oxidized layer. This HF-etched n-doped wafer is presented in table 6.1 as sample hfn0. From the same table we can see that the pump reflection changed radically, from 9-35 %, as a result of removing the passivated layer. Pump-probe measurements were performed on the bare HF-etched wafer and the results can be seen in table 6.2. As we expected, the $\Delta R/R$ was reduced, by as much as 55% for s-polarized probe light. This observation emphasises the large influence of passivation on $\Delta R/R$.

6.3.5 Incident angle and passivation layer thickness

The correlation between the choice of incident angle and the passivation thickness and how this effected the reflectivity, was analysed for a range of input parameter, based on Abdulahim's algorithms for multilayer wafers in reference [4]. In this analysis the probe incident angle was set to 45° and the pump angle to 5°, to describe our experimental setup. The type of passivation layer (Si3N4 or SiO2) was taken into account, and from this the probe and pump reflectivities were found for a range of passivation layer thicknesses. The results for nitride and oxide wafers are presented in figure **??**.

The figures show how the reflectivity has a cosine dependence with respect to passivation layer thickness. This means that the passivation layer thickness may be adjusted to a thickness located at a minimum or maximum of the reflectivity. Our previous measurements showed how a smaller pump reflection gave a lager $\Delta R/R$. With this in mind, we would expect the maximum excitation density to be generated at a minimum on the reflectivity curve. This analysis propose that this can be achieved by adjusting the passivated layer thickness. In the same way, this might be done for a range of incident angles, by setting the passivation thickness unchanged. Hence, the pump incident angle may be adjusting to an angle which corresponds to minimum reflectivity.

The probe beam reflectivity (in figure 6.5b and 6.5d) follows a similar cosine curve as the pump beam. The incident angle of 45° give rise to a significant different reflectivity curve for s- and p-polarized probe beams. The probe beam reflectivity may be adjusted to a suitable level for the setup, aiming to improve the signal-to-noise ratio. This is however subject for future studies, and may be of great importance to improve the experimental setup.

The measured pump reflection from the passivated wafers, presented in table 6.1, may be related

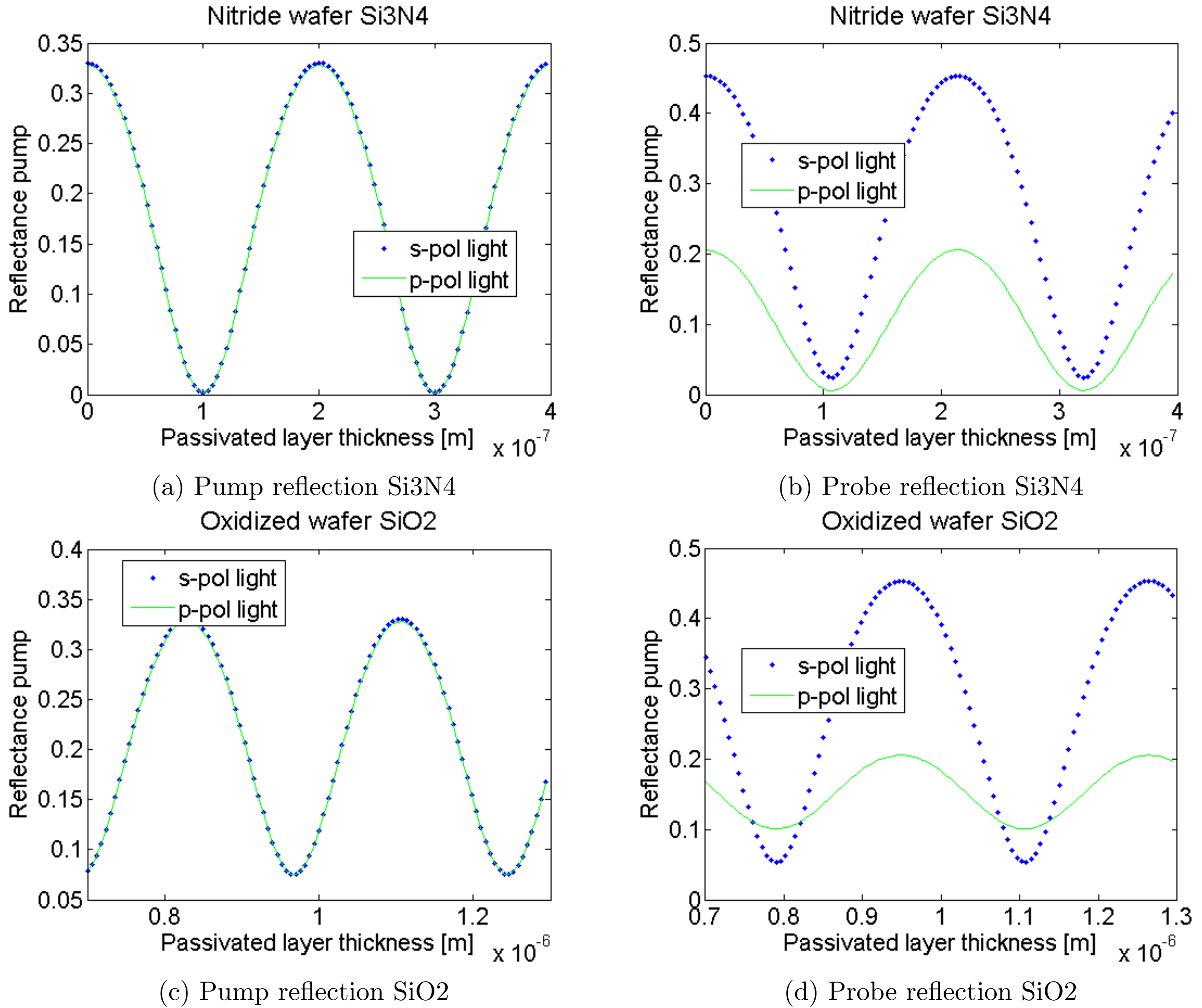

(a) Pump reflection Si3N4

(b) Probe reflection Si3N4

(c) Pump reflection SiO2

(d) Probe reflection SiO2

Figure 6.5: Presents the calculated reflectivity for pump incident angle 5° and probe incident angle 45°, over a range of passivation layer thicknesses. The results are shown for passivated nitride wafers Si3N4 and oxidized SiO2 wafers.

to the figures in **??**. The thickness of the nitride passivated Si wafer, nitp0, in this work was adjusted to 156 nm. From figure 6.5a this thickness corresponds to a reflectivity of around 22%, which is in the middle of the maximum and minimum reflectivity possible to achieve. The oxn0 wafer showed a significant smaller measured reflectivity in table 6.1 than the other wafers. In figure 6.5c the passivation thickness 986 nm (for oxn0) corresponds to a minimum reflection of around 8-9 % reflection, which is in good agreement with the measured result. Hence, the passivation thickness for oxn0 in combination with the incident angle of 45° gave the lowest possible pump reflectivity for this sample. This is however not the case for other wafers, and may explain why the passivated wafers showed a wide range of reflections in table 6.1.

6.4 Crystal orientation

As discussed in the previous chapter, pump-probe measurements were performed with the wafers rotated 90° around their azimuth. The results showed significant changes in $\Delta R/R$ values after the wafers were rotated. However, as the $\Delta R/R$ value increased after rotation for some wafers and decreased for others, no conclusion can be drawn from this. The possible reasons for the large variations in measured $\Delta R/R$, is discussed in section 6.4.1.
A wafer rotation of $90^{degrees}$ for a (111) wafer would change the crystal plane parallel to the pump polarization, from the (110) to the $(22\bar{1})$ plane. The result from pump-probe experiment performed on the rotated ox1 (111) wafer, showed a reduction in $\Delta R/R$. However, we experienced a relatively large variation in measured values for the (100) wafers, which reduces the certainty of this single observation. Since this measurement was only performed on one rotated (111) wafer, the result is inconclusive.

However, further measurements should be performed to investigate the relation between crystal orientation and laser beam polarization. Samples of different crystal orientations may be studied as well as other rotation angles. Eg. rotating a (100) wafer 45° will change the crystal plane parallel to the pump polarization from the <110> to the <001> direction. This may explore the potential for using pump-probe experiment to characterise crystal orientations in a sample.

6.4.1 Variations in measurements

During the measurements, we experienced that results changed from one measurement to another if the wafer was removed and put it back in before the next run. These variation from one measurement to another was first studied by performing a series of nine identical pump-probe measurements of the exact same spot, without removing it between each scan. The measurements were carried out on the oxide wafer, ox1. The resulting $\Delta R/R$ value for each measurement is shown in figure 6.6. The results are nearly identical with a minimal change from one measurement to the other. This indicates that long-term pump power exposure or internal changes in the material may not contribute to the observed variation in $\Delta R/R$ values.

The signal to noise ratio (SNR) and the dynamic range (DR) can be found from the nine identical measurements. The SNR and DR are defined in Naftaly and Dudley's paper [20] as

$$SNR = \frac{mean\ magnitude\ of\ amplitude}{standard\ deviation\ of\ amplitude} \tag{6.1}$$

$$DR = \frac{maximum\ magnitude\ of\ amplitude}{rsm\ of\ noise\ floor} \tag{6.2}$$

From our series of measurements, which may represent a typical pump-probe experiment for our setup, we found SNR = 51.42 and DR = 202, and a noise level of $\sim 2.5 \times 10^{-7}$.

The results presented in table 6.2 are the best results we achieved. In addition, a large range of results were generated throughout this work, creating a large cap in the measurements. One explanation is that our experimental skills and experience have improved a lot during the period,

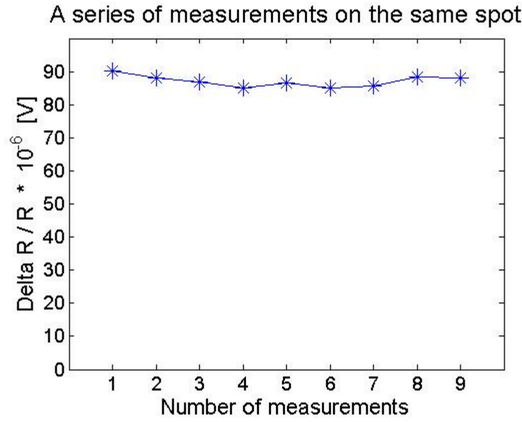

Figure 6.6: $\Delta R/R$ results from a series of nine pump-probe measurements performed at the exact same spot of wafer ox1, carried out right after each other.

making better results. However, measurements performed within the last period show large variations when the wafer is removed and put back in the setup, or the a new spot on the wafer is used.

For each time a wafer was removed and then put back in the setup, the measured $\Delta R/R$ value changed slightly or significantly. This was observed for measurements performed with the parallel pump and probe polarizations as well as for orthogonal polarizations. Some wafers were removed and then remeasured several times, while others were only measured in then same wafer position without any changes. Figure **??** illustrates the range of measured $\Delta R/R$ values for each wafer, with the probe parallel and perpendicular to the pump. The main observation is the large variation from one measurement and another, if the sample's position is slightly changed. This is of great importance since it points out the large uncertainty in our obtained pump-probe results.

Comparing figure 6.6 and 6.7b gives us confidence in the measurments performed on the same spot without any experimental changes. Hence, the variations from one measurement to another performed on the same spot, are negligible compared to the wide range of results obtained when the sample position is changed.

One possible explanation to the wide range of obtained $\Delta R/R$ results, is based on the pump beam's Gaussian shape. Since the pump beam is not uniformed distributed, but rather Gaussian shaped, the spatially variation in pump intensity may give rise a wide range of results. Depending on where the probe beam is located within the Gaussian shaped pump beam, the results presents the pump intensity within this region. Throughout the experiments, we adjusted the probe beam in such way that it hit within in center of the pump beam. However, this was measured by eye and a large uncertainty must be taken into account. Small, not even visible, changes in the probe beam position within the pump beam, will give a slightly different intensity distribution and hence, a different $\Delta R/R$ value. The largest intensity distribution is found when the probe beam is located in the center of the Gaussian shaped pump beam.

The discussion above may explain the large variation observed in figure 6.7a and 6.7b, since the probe position within the pump beam might have been slightly different every time the wafer was removed and then remeasured. This also points out that our results presented in table 6.2 are not necessarily comparable, since the probe location within the pump might be different for

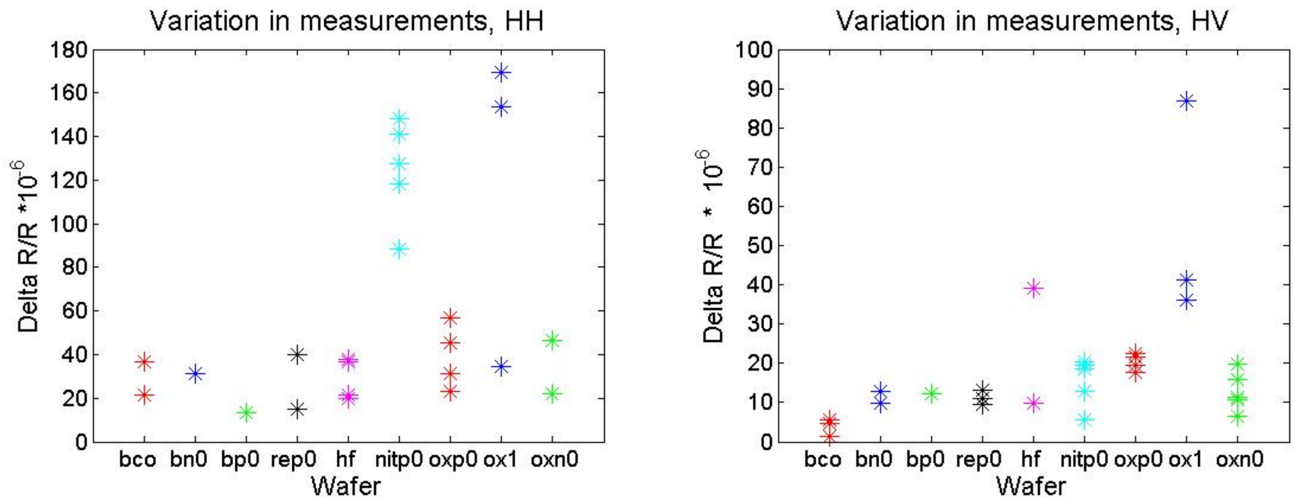

(a) Parallel pump and probe polarization.

(b) Orthogonal pump and probe polarization.

Figure 6.7: Illustration of the measured $\Delta R/R$ values obtained for each wafer, when the wafer was removed and then put back in the setup.

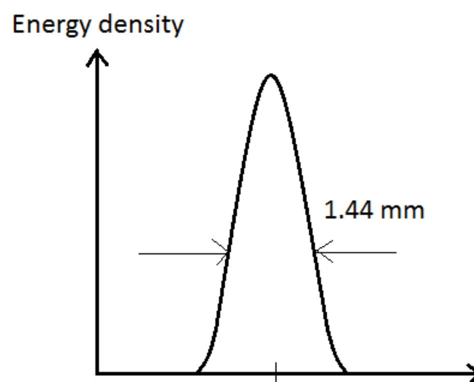

Figure 6.8: Illustration of the Gaussian shape pump pulse.

each measurement. This is an important element which should be taken care of in future studies. However, since several measurements are performed for each wafer, we still believe in the overall picture presented in table 6.2, showing a larger $\Delta R/R$ for the passivated wafers.

The variation might also be due to real changes in the wafer from one spot to another, or from small external perturbations giving rise to variations in the results.

To achieve more accurate and comparable results, the experimental pump-probe setup should be improved to create a more uniform pump pulse distribution. This will eliminate the large spatial intensity variations from the results.

6.5 Quantum efficiency

The number of excited electrons may be found from the excitation density, given in table 6.2, and the effective volume in the samples, which was found in the previous chapter as $V = 1.63 \times 10^{-5}\ cm^3$. For sample oxn0, with excitation density $6.8 \times 10^{18}\ cm^{-3}$ for parallel probe polarization, the number of generated carriers is

$$N = n \cdot V = 6.8 \times 10^{18}\ cm^{-3} \cdot 1.63 \times 10^{-5}\ cm^3 = 1.1 \times 10^{14}\ \ electrons \tag{6.3}$$

The external quantum efficiency (QE) gives a ratio of the material's performance and may be used for solar cell applications. The number of photons in the pump beam was found in section 5.5.2, as 4×10^{14}, and the external QE can then be calculated for wafer oxn0,

$$QE = \frac{1.1 \times 10^{14}}{4 \times 10^{14}} = 27.5\% \tag{6.4}$$

However, the variations in measured $\Delta R/R$ give rise to a wide range of quantum efficiencies. Hence, the QE is not a good measure for the performance of the material for our setup, since the values are not directly comparable.

6.6 Multicrystalline Si

The pump-probe measurements of the multicrystalline wafers were performed in the same way as for single crystalline samples. The goal was to investigate the carrier dynamics and the number of carriers generated, by measuring the $\Delta R/R$. The purpose was also to study local difference on the wafer, between grains to their grain boundaries.

The complex crystal orientations of the mc-Si wafer, made the experimental technique challenging. The size of one grain varied, from 10 mm to around 1 mm, which required a complete control of the pump beam position on the wafer. The small margins from one grain to another, made the experimental technique demanding in order to perform accurate measurements within a grain, or exactly on a grain boundary. The grain structure could not be seen on polished side of the wafer, where we performed the measurements. The complexity of mc-Si, made the error and uncertainties significantly higher than for single c-Si. However, the achieved experimental knowledge from measurements on single c-Si was crucial in developing a best suitable technique for the mc-Si samples. From the first pump-probe measurements on mc-Si to the final results resented in this section, the improvements are remarkable. Nevertheless, future experiments should aim to develop an advanced and sophisticated pump-probe technique designed for mc-Si samples, to achieve more accurate results.

Since the crystal structure for the mc-Si wafers were inhomogeneous and varied from one grain to the other, defining the crystal direction parallel to the pump polarization was not relevant for mc-Si.

6.6.1 Measurements of mc1

Within grains

The first measurement was restricted to study a spot located within a grain on mc1. The setup was adjusted such that the pump and probe beams would hit within the center of the selected grain, and away from its grain boundary. Measurements were performed with pump and probe polarizations parallel and perpendicular. Figure 6.9 presents the results from measurements within one grain.

From figure **??**, with orthogonal pump and probe polarizations, a fast decay in the reflected signal can be observed. The initial negative change in reflectivity due to the pump excitation, has an immediately fast recovery within the first picosecond. This transient stabilizes after tens of picoseconds. Such fast initial recovery was not observed from the previous single c-Si results.

An important observation when comparing the results for parallel and perpendicular probe polarizations, is how coherent artifacts dominates within the first picoseconds when the pump and probe polarizations are parallel, figure 6.9a. This clearly reduces the ability to study the fast decay behaviour. The coherent artifacts are eliminated from the measurements with orthogonal pump and probe polarizations, and this allow us to investigate important carrier dynamics during the

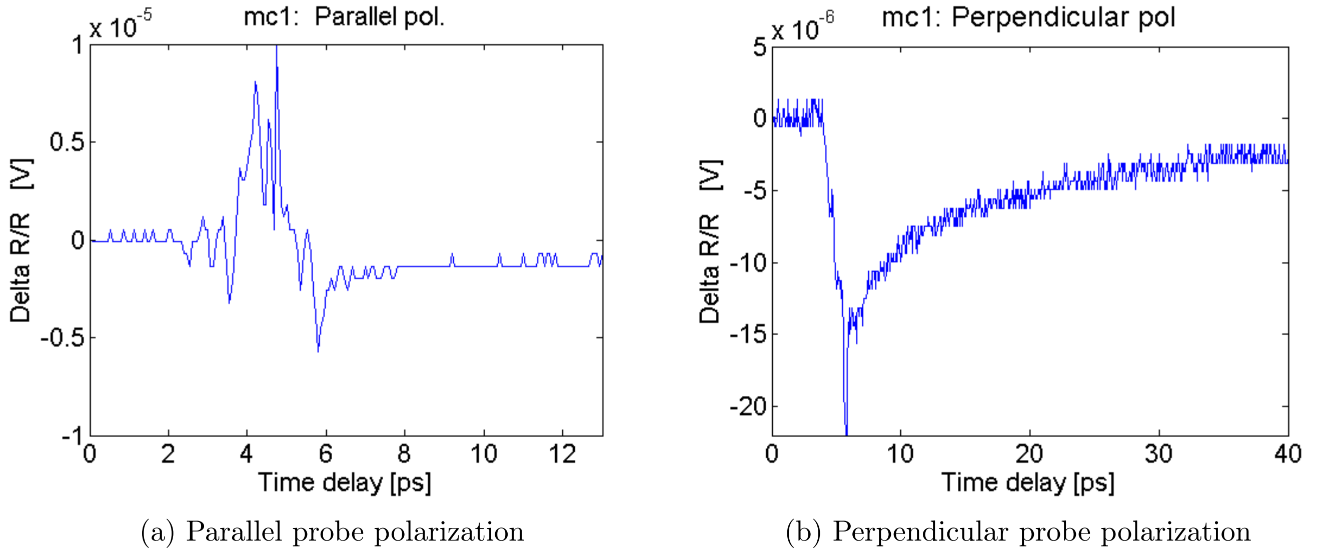

(a) Parallel probe polarization

(b) Perpendicular probe polarization

Figure 6.9: Pump-probe measurements performed within a grain on sample mc1.

first few picoseconds. Consequently, the following experiments on mc-Si wafers were carried out with the probe polarization perpendicular to the pump.

The result seen in figure 6.9b is of great interest since it provides details about the abnormal carrier dynamics taking place in the mc-Si sample. The initial reflection recovery observed is equivalent to a fast reduction in the generated carrier density. From measurements performed on single c-Si in section 6.3, we expect carrier lifetime in the order of μs for c-Si. Hence, we propose that the fast reflectivity decay is due to trapping of photoexcited carriers into trap states within the bandgap. Since free carrier describe by Drude model contributes to a reduced reflection, the observed ultrafast trapping of carriers must be the dominant characterization of the reflected signal. This interpretation is supposed by conclusions in the work from Jepsen et al. (in reference [25]) and Macdonald et al. (in [25]). They observed the same fast decay feature in mc-Si samples. These observation are of great interest for solar cell applications, as the trapped carriers will reduce the material performance.
The fast decay time related to trapping of carriers, may be calculated by polynomial curve fitting. The decay time in figure 6.9b is found to 4.4 picoseconds. However, there seem to be more than just one exponential decay describing the recovery curve. This will not be examined in this work, but for a better understanding of the carrier dynamics taking place in mc-Si, this should be analysed in future studies.

The recovery of the reflected signal may be found by comparing the initial $\Delta R/R$ value with the recovered reflection. Hence, $\frac{14.5-2.5}{14.5} = 0.83 = 83$ %. This indicates that 83% of all the photogenerated carriers are trapped within the first picoseconds. Table 6.5 presents the results from the mc-Si samples, showing the calculated excitation density, fast decay time and trapping density.

The level where the reflection transient stabilizes is determined by the number of generated carriers and the trapping density. At this level the trap states are filled up, and the dominant process is

expected to be radiative carrier recombination. If the trap states are shallow traps, the carriers may relax to the valence band again, while for deep traps the carriers can recombine with carriers of opposite charge in the trap state.

To support the results done within one single grain, another grain located on the other side of the mc-Si wafer was examined. This way, local differences could be observed as the crystal structure and density of defects may vary from one grain to another [19]. The result can be see in figure 6.10 and a fast reflection recovery can be observed. This is similar to the previous result within another grain on the wafer, and suggests that the fast decay feature is not only a local observation.

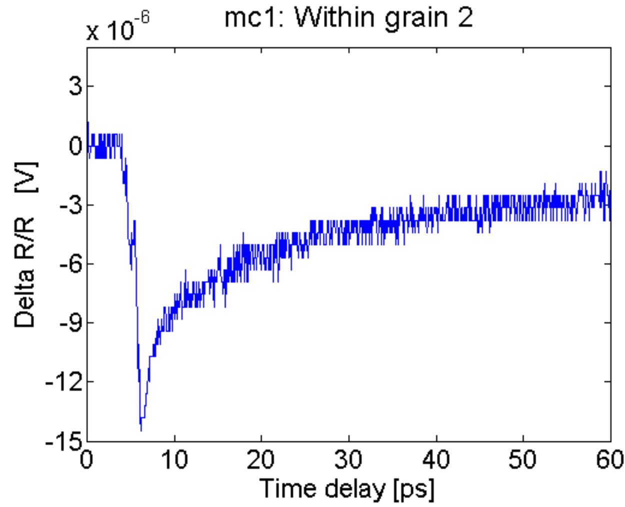

Figure 6.10: Pump-probe measurement performed within grain number 2 on wafer mc1.

Table 6.5: Results from pump-probe measurements performed on mc-Si wafers, within grains (WG) and at grain boundaries (GB). The table presents the values for $\Delta R/R$, excitation densities, fast decay time, the reflection recovery (in %) and the trapping density.

Sample	**Area**	**Probe reflection**	**Δ R /R ×10^{-6}**	**Excitation density [cm^{-3}]**	**Decay time**	**Reduction in %**	**Trapping density**
mc1	WG 1	0.38	14.5	4.1×10^{18}	4.4 ps	83%	3.4×10^{18}
	WG 2	0.38	13.7	3.9×10^{18}	6.6 ps	80%	3.1×10^{18}
	GB 1	0.38	14.5	4.1×10^{18}	4.2 ps	85%	3.5×10^{18}
	GB 2	0.38	10.5	3.0×10^{18}	2.3 ps	87%	2.2×10^{18}
mc2	WG	0.38	14.7	4.2×10^{18}	-	-	-
	GB 1	0.38	11.1	3.2×10^{18}	-	-	-
mc3	n/a	0.38	5.3	1.5×10^{18}	1.2 ps	87%	1.3×10^{18}
mc4	n/a	0.38	15.8	4.5×10^{18}	6.0 ps	96%	4.3×10^{18}

Grain Boundaries

The experiment then proceeded to study a grain boundary, between two grains on the wafer. The setup was adjusted so the pump beam hit on each side of the grain boundary, making sure the pump straddled. Measurements were performed on two different grain boundaries, located on each side of the wafer. Each grain boundary was connected to one of the grains used in the foregoing experiments, to examine any noticeable change between a grain a its grain boundary.
Figure 6.11 show the experimental results. An initial fast recovery in the probe transient can be

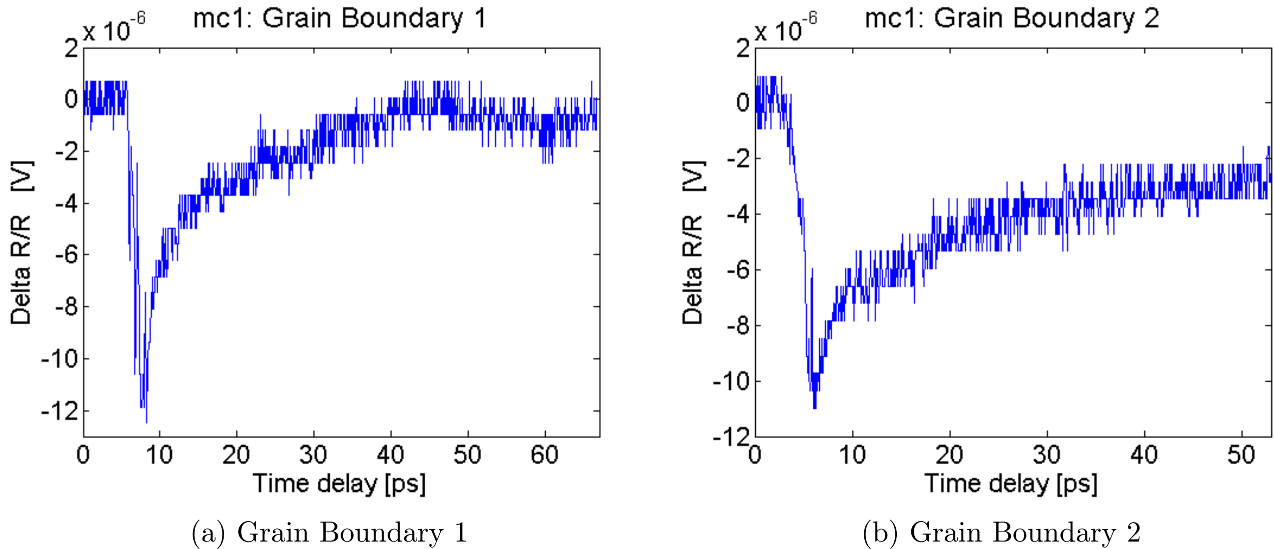

(a) Grain Boundary 1

(b) Grain Boundary 2

Figure 6.11: Pump-probe measurements of grain boundaries on sample mc1.

observed for both grain boundaries. Hence, a ultrafast trapping of carriers is observed for all the measured areas on the mc1 wafer. Table 6.5 provides further numerical results.

6.6.2 Measurements of mc2

Measurements of the mc-Si sample mc2 were performed in the same way as for mc1, for one grain and on a grain boundary. Figure 6.12 shows the results, and no fast recovery can be observed for the grain or the grain boundary. This is similar to the results we obtained for single crystalline Si wafer.

6.6.3 Measurements of mc3 and mc4

Mc3 and mc4 were from the same ingot, and were sawn in such way that the grains could not be seen. Pump-probe measurements of mc3 and mc4 aimed to look for fast decay feature on the wafers, regardless if the measurement was carried out on a grain or a grain boundary. Two different spots on each wafer was measured, and they all showed a short recovery features, see figure 6.13. Hence, three out of four mc-Si samples showed trapping of carriers taking place within tens of picoseconds. This emphasizes how detailed knowledge about the carrier dynamics in mc-Si is crucial when analysing the material for solar cell applications.

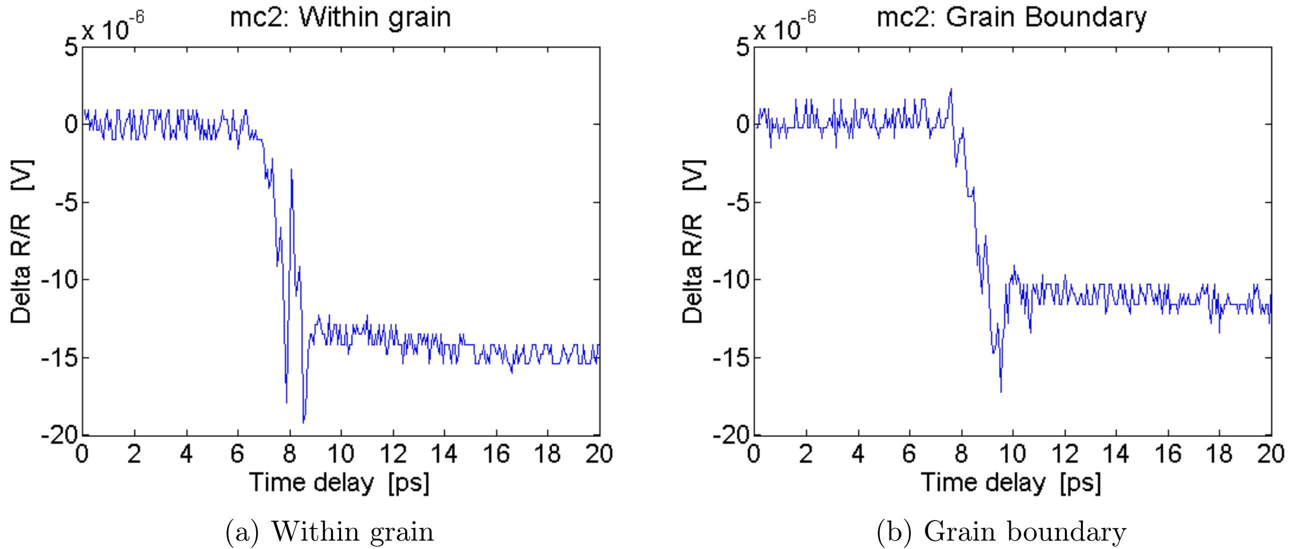

(a) Within grain

(b) Grain boundary

Figure 6.12: Pump-probe measurements of sample mc2.

From table 6.5 it can be see that the observed reflection recoveries of the mc-Si wafer are between 80-96 %. This corresponds to a trapping density in the same order as the excitation density, leaving a very few carriers left in the valence band. The trapping densities are found in the range $(1.3 - 4.3) \times 10^{18}\ cm^{-3}$. No noticeable difference can be observed between measurements of grains and grain boundaries.

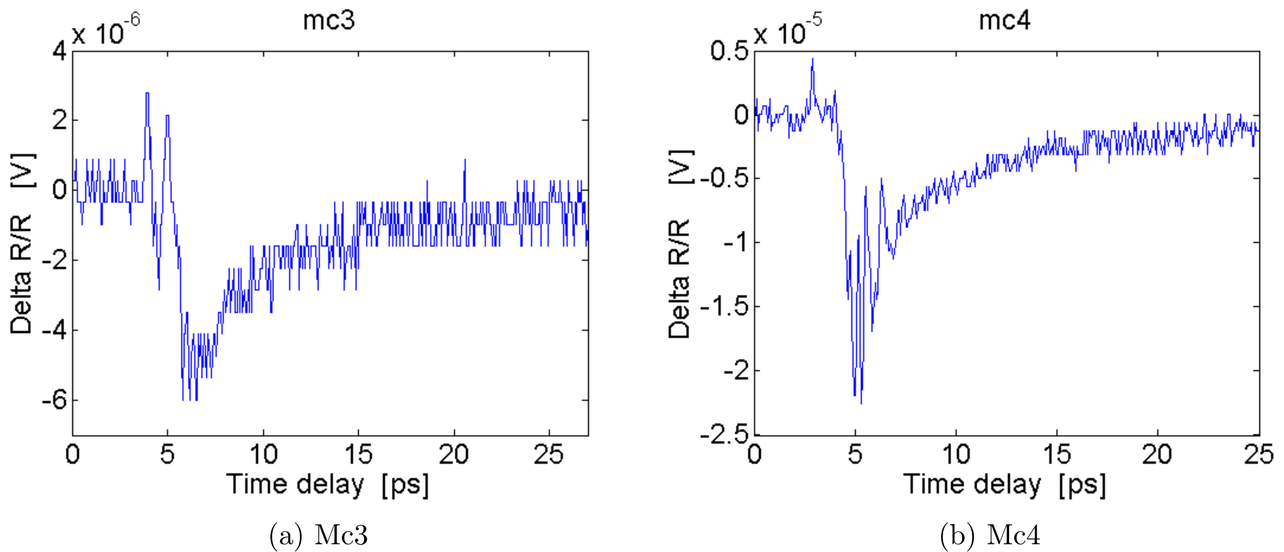

(a) Mc3

(b) Mc4

Figure 6.13: Pump-probe measurements of the samples mc3 and mc4.

6.6.4 Causes of defects

Trapping densities in mc-Si samples are typically larger than in single c-Si due to crystal defects and lager impurity concentrations. For further details about defect and impurities in silicon, see section 3.3.1. For solar cell applications, trapping of carriers is important since it decreases the

number of generated carriers available and reduces the solar cell performance. In the following sections, we will discuss the possible causes of the observed defects, aiming to address their origin.

Polishing defects

The polishing process may cause defects in the crystal. To investigate this, a measured wafers which showed no such defects before was repolished to see if a different result could be observed. The technique used was an automatic polishing machine at Sintef Trondheim. After repolishing, a pump-probe measurement was performed with the pump and probe polarizations orthogonal. The result can be seen in figure 6.14. No fast recovery or defect behaviour can be observed as a result of polishing. Hence, this experiment indicated that the polishing process might be eliminated from the possible cause to short decay behaviour. However, we are lacking the detailed information about how the mc-Si wafers used in this work were polished. Different polishing methods than the one used in this experiment, might affect the result and a final conclusion cannot be drawn before the detailed knowledge about the wafers is presented.

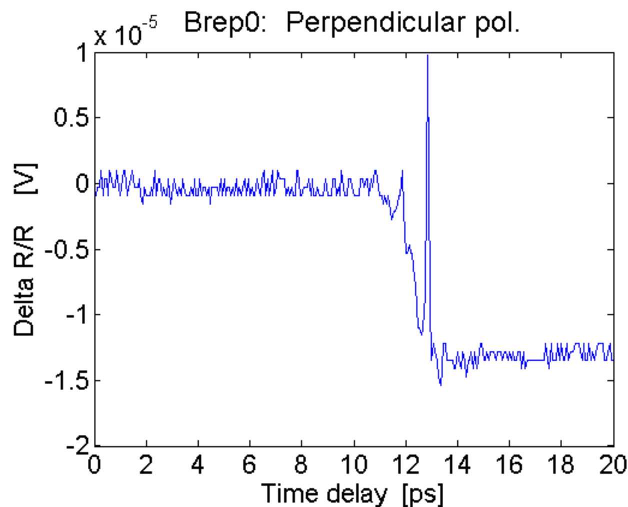

Figure 6.14: Results from pump-probe measurement performed on a repolished wafer. The probe beam polarization is parallel to the pump beam.

Structural defects

To study the possible defects from crystal orientations and structural defects that might cause trap states, a EBSD mapping was performed at Sintef Trondheim. See Chapter 5 for more details about EBSD mapping. The motivation was to look for crystal defects that might occur in mc-Si, to see if these effect contributed to the pump-probe measurements. EBSD mapping was restricted to only one grain and one grain boundary on the wafer mc1. Figure 6.15 presents the result. The drawn circles correspond to the areas where pump-probe measurements have been performed. Within the marked grain, no crystal defects can be observed and the grain has a homogeneous crystal structure. The marked grain boundary shows a clear edge between two defined crystal structures. Hence, the EBSD mapping indicates that the observed ultrafast trapping of carriers is not attributed to crystal defects.

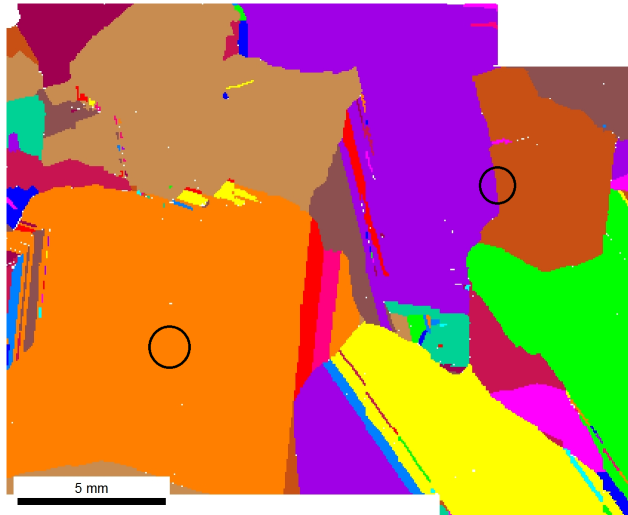

Figure 6.15: EBSD mapping of sample mc1. The circles presents areas where pump-probe measurements have been performed.

Surface states

Since the samples mc1, mc3 and mc4 are non-passivated wafers, a possible source of defects might be dangling bonds at the bare wafer surface. These unpaired bonds, described in section 3.3.2, may create energy levels within the band gap and give rise to trap states. However, our results from pump-probe measurements on bare single crystalline Si, did not show effects of trap states. This observation was also supported when removing the passivation layer of the oxn0 sample, did not show defect behaviour. This indicates that the observed trapping in mc-Si is not a only a result of surface states in the bare wafer. However, the origin of the defect states are challenging to investigate and beyond the scope of this theses. For future studies, the contribution of surface states may be studied by passivating the wafer, which will reduce the surface dangling bonds. Performing new measurements and comparing the results, may indicate how the trap states are related to surface defects.

6.7 Conductivity analysis

THz TDS measurements (see chapter **??**) were performed on four wafers: bn0, oxn0, nitp0 and mc1. The results provided information about the refractive index, the absorption coefficent and the frequency domain over the range 0.5-2 THz. From this, the optical static conductivity and mobility may be calculated through the equations stated in Chapter 4.

Since the doping concentration of the wafers were unknown, we estimated a carrier density n_{eq} in equilibrium to set a value for ω_p^2. This was done by fitting

$$\sigma_r = 2n_r n_i \epsilon_0 \omega \tag{6.5}$$

where n_r and n_i were parameters we obtained from THz TDS measurements, to

$$\sigma_r = \frac{\epsilon_0 \omega_p^2 \tau}{\omega^2 \tau^2 + 1} \tag{6.6}$$

Combining the two equations, we got

$$(2 n_r n_i \epsilon_0 \omega) \cdot (\omega^2 \tau^2 + 1) = \epsilon_0 \omega_p^2 \tau = \sigma_{dc} \tag{6.7}$$

To find the intersection between the left and right side in equation 6.7, the collision time τ was found from the literature, and set to τ = 90 fs which Titova and Hegemann found in reference [37]. The carrier density n_{eq} was then adjusted for the curvature of the left side in 6.7 to intersect with the constant value of the right side. This gave us the static conductivity σ_{dc} and the mobility was found from the relation $\mu_e = \frac{\sigma}{nq}$ (for an n-doped material). The results are presented in table 6.6.

Table 6.6: Estimated static conductivity σ_{dc} and mobility μ from THz TDS results. The values for carrier density n_{eq}, collision time τ and ω_p used in the estimation are also presented.

Wafer	**Area**	τ	$\mathbf{n_{eq}}$ **[cm^{-3}]**	$\omega_\mathbf{p}/\mathbf{2}\pi$**[THz]**	$\sigma_\mathbf{dc}$ **[S/cm]**	μ **[cm^2/Vs]**
bn0		90 fs	4×10^{13}	1.09	38.9	608
oxn0		90 fs	3×10^{13}	0.95	29.2	608
nitp0		90 fs	5.5×10^{13}	1.08	37.6	428
mc1	WG	90 fs	7×10^{13}	1.22	47.9	544
	GB	90 fs	8×10^{13}	1.30	54.7	622

In comparison, Titova and Hegemann found a mobility of $\mu = 500 cm^2/Vs$ for silicon, which is within the range of mobilities we found in table 6.6. Jeon and Grischkowsky studied p-doped silicon with a resistivity of $\rho = 9.6 \Sigma cm$ in reference [16], and used $n_{eq} \sim 9 \times 10^{14} cm^{-3}$, which gave $\omega^2/2\pi = 0.45\ Tz$ as fitting parameter. They obtained a mobility $\mu = 730 cm^2/Vs$ for the p-doped Si. For our p-doped silicon samples we found a mobility in the range $428 - 622 cm^2/Vs$, which is smaller than Jeon and Grischkowsky obtained, but still within reasonable agreement since our samples might be of different resistivity and have other types of doping components.

The doping concentration N_a of nitp0 may be calculated from the known resistivity, to see if it's in agreement with our fitting parameter n_{eq}. This is done by using the computation method in reference [1] for boron-doped Si, which states that

$$N_a = \frac{1.33 \times 10^{16}}{\rho} + \frac{1.082 \times 10^{17}}{\rho[1 + (54.56\rho)^{1.105}]} \tag{6.8}$$

Inserting the nitp0 minimum resistivity of $10 \Sigma cm$, we get

$$N = 1.34 \times 10^{15}\ cm^{-3}$$

This is more then ten times larger then the carrier density we used in table 6.6 for nitp0 and indicates that our fitting parameters might be adjusted for better suitable values. By inserting the

calculated doping concentration as a fitting parameter n_{eq}, we get a $\tau \sim 4$ fs, suggesting that the collision time τ for the nitp0 sample might be less than 90 fs.

From table 6.6, the mobilities for bare and passivated n-doped silicon are found to be the same, 608 cm^2/Vs. The p-doped nitp0 has a lower mobility, which was expected since holes have a smaller mobility then electrons. However, since the resistivity of oxn0 and nitp0 is in the same order, we would expect this difference to be even larger. Jeon and Grischkowsky found the mobility for an n-doped Si sample, with a resistivity in the same order as oxn0, to be $\mu = 2000$ cm^2/Vs. To investigate this, further THz-TDS measurements should be performed for a range of n- and p-doped materials. Worth mentioning is also the observed difference in mobility for grain and grain boundaries. Further analysis is, however, outside the reach of this theses, but should be subject for later research.

Chapter 7

Conclusion

In this work, pump-probe experiments were carried out for a range of c-Si wafers, by measuring the probe reflection from the samples. The purpose was to explore the used of pump-probe measurements to study carrier dynamics in mc-Si. Measurements of single c-Si samples were used as a basis in this work. The measured $\Delta R/R$ was also studied for a range of input parameters.

Passivation was observed to have a large impact on $\Delta R/R$. The passivated wafers showed smaller pump reflection, larger excitation densities and increased $\Delta R/R$ compared to non-passivated wafers. To observation was supported by etching off the passivated layer of an oxide (SiO2) wafer. The outcome showed a radically increase in pump reflectivity from 9% to 32%, and the excitation density was reduced. Analysis showed that the incident angle on a passivated wafer may be chosen such that the pump reflection loss is at a minimum. This provide great manual control over the reflection loss in the setup.

A large variation in $\Delta R/R$ was observed for measurements performed before and after the wafer was removed and then put back into the setup. This worked suggested that the main explanation was grounded in the Gaussian shaped distribution of the pump beam. For a series of measurements performed with the sample unchanged in the same position, the small variations between each run were negligible compared to the uncertainty related to the position of the probe beam within the Gaussian shaped pump beam. A more uniform distributed pump pulse was recommended to achieve comparable results.

The best suitable experimental setup for studying carrier dynamics in mc-Si, was found for perpendicular pump and probe polarization. This allowed us to observe interesting carrier dynamics within the fist picoseconds, which otherwise were dominated by coherent artifacts. A fast initial recovery of the reflected signal was observed for mc-Si wafers. We attributed the fast decay to trapping of carriers, which is of great interest when analysing mc-Si for solar cell applications. The reflected signal recovered more then 80% within the first 30 ps, which resulted in trapping densities in the same order as the excitation densities.
Possible crystal defects in a mc-Si sample were examined by an EBSD mapping, and defect occurring during a polishing process were studied. However, this work was not able to address the

origin of the observed defect states in mc-Si.

In this these we have established a methodology for using pump-probe measurements to analyse mc-Si samples. We have shown how this technique may be used to attribute defects, e.g. whether they derive from electrical or optical properties, which is of great interest for improving the efficiency of low cost solar cells. The contribution from a range of input parameters to $\Delta R/R$ studied in this theses, may be used as a baseline for improving the experimental setup in future studies.

Chapter 8

Future work

Future pump-probe measurement should aim to develop an improved experimental setup, for more accurate and reliable results. From what we experience in this work, one of the main improvements will be to create a more uniform distributed pump pulse. This may be done by using a top hat beam shaper to reduce the spatial variations in pump intensity. Another option might be to reduced the pump diameter for a more defined peaked pulse in space, and by scanning the probe beam across the material, the spatial variation may be reduces. In addition, the best suitable ratio of the pump and probe areas should be developed, in order to have a small enough probe to be sure it's located within the pump area, but at the same time reduce the spatial variation with the pump pulse.

In this theses we started an analysis of how the reflectivity of passivated samples varies with passivation layer thickness and incident angle. This study should be continued in future research, aiming to find the best suitable experimental setup for each passivated sample. The signal-to-noise ratio should be improved by determining the best combination of pump and probe beam reflectivity.

Further research should be done on how different crystal directions parallel to the pump polarization affects pump-probe measurements. Wafers of different crystal structures may be used, as well as other rotation angles. E.g. rotating a Si(100) wafer 45° will change the crystal direction parallel to the pump from <110> to <001>. In order to study how initial transients within the fist picosecond may change, we recommend an experimental setup with perpendicular pump and probe polarizations to reduce coherent artifacts within this time domain. Future research may explore the possible use of pump-probe technique to characterize crystal structures, which is of great interest for multicrystalline materials.

For a better understanding of mc-Si, the fast decay feature observed in this work, should be investigated in future research. Aiming to address the defect states observed in mc-Si, may also provide detailed information about how to remove the defects and hence, increase the material performance. This will be of great interest for mc-Si solar cells. To begin with, the contribution from surface states may be identified by passivating the mc-Si samples, to see this reduces the trap state density. The defect states might occur during sample preparation, and for a more systematic research, a range of sample parameter should be included in the study; such as doping

atoms, growth method, grain size and wafer's history. In addition, the experimental pump-probe technique for mc-Si should be improved, to obtain a better control of where the pump and probe pulses are located relative to the grains on the wafer. This will ensure more reliable results and a good basis for further studies.

Appendices

Appendix A

Lock-in amplifier

A.1 Lock-in theory

A description of the how the lock-in amplifier works, may be given through four stages: The first stage is the ac amplifier or the signal amplifier and it is a voltage amplifier with a filter. The second stage is the voltage controlled oscillator (VCO) and can coordinate the phase and the frequency with the reference signal. The third stage is the phase sensitive detector (PSD) which is the heart of a lock-in amplifier. The fourth stage is a low-pass filter which ignores frequencies outside the region of interest. The last stage is the dc amplifier that amplifies signals at low frequencies.

The reference signal is set at the voltage controlled oscillator and the frequency is set to the frequency which corresponds to the input signal. The reference signal also contains a phase difference θ between the two signals. The reference signal could look like this:

$$V_{VC0}(t) = V_0 \cdot cos(\omega_r t + \theta) \tag{A.1}$$

The next stage is the PSD where the input signal and the reference signal are multiplied together and the output is the product of two sinusoidal waves. This might be represented as two ac signals which is a sum of two new sinus waves. The new frequencies depends on $(w_0 - w_r)$ and $(w_0 + w_r)$. In this case the two frequencies are equal, so the output will contain two terms; one for the second harmonic and the other for dc. The amplitude of the two terms are both propotional to the input signal amplitude V_0.

The next stage in the lock-in is the low-pass filter and the signal is sent through. The filter removes the second harmonic term and keeps the dc term. The dc signal is then amplified to a sufficient level in the dc amplifier. The final output will be a dc term proportional to the input voltage we are interested in.

From this we can see that in order to obtain a dc signal the phase between the two signals needs to be synchronized such that the phase difference is constant. The reference signal therefore has to be phase-locked to the input signal. This explains the name of the amplifier. Changes in the

input signal does not change the measurements since the reference is phase-locked to the input. The combination of the low-pass filter and the phase sensitive detector makes it possible to ignore large amplitude noise even if the frequencies are close to the signal frequency but not phase locked to the signal [41, 34, 31].

A.2 Procedure to reset the lock-in amplifier

This appendix outlines the procedure of how to use the lock-in amplifier for pump-probe experiments described in the report.

1) Reset
Disconnect all cables from the lock-in. When turning on the lock-in amplifier the [Setup] button must be hold down while the lock-in is starting up. This is to reset the aperture and deleted previous data and setups from earlier measurements.

2) External reference
It is importnat that the settings are assigned to take a reference signal as an input and not an internal signal generated in the lock-in. Hence, make sure the light Internal unser Source is OFF. Push the button so the Pos edge is ON. An external reference signal can now be measured. To check that the detector detects the desire signal and the chopper signal works propely, connect both of them to an oscilloscope to make sure the signal are connected.

3) Set the reference signal
Next step is to set the reference signal. To do so, the detector must connect to the lock-in through the A/I input. Reference frequency: the chopper is connected to the Ref In input on the lock-in amplifier through the frequency generator. Reference phase: Since only the pump is passing through the chopper, the pump pulse must be used in order to set the reference phase. Hence, the probe is blocked and only the pump pulse is measured. This may be done in different way, but usually the scattered pump light from the sample reaching the detector is enough to set a reference signal, so no setup change is required. The detector is connected to the lock-in through the A/I input, which shows the pump signal as function of X and Y, or R and θ. The reference phase is set by following the steps below:

Press [Auto phase]. This automatically adjust the reference phase shift to eliminate any residual phase error. This should set the value of Y to zero. This should also change the reference phase shift to a value which may be negative or positive.

Press [+90 degrees]. This adds 90 degree to the reference phase shift. The value of X drops to zero and Y becomes the magnitude. (X and Y switch values so that X = Y and Y = -X). Use the knob to adjust the phase shift until Y is zero and X is equal to the positive amplitude. The sensitivity may be adjusted for more accurate numbers on the displays.

Press [Auto Phase], which sets the reference signal and adjusts the X and Y values.

4) Set important parameters

Some parameters need to be set to a suitable value to make a good measurement. Sensitivity and Time Constant are of great importance and should be chosen such that the noise is small (usually this means longer Time Constant) and the sensitivity is high enough to detect the signal, without reaching saturation in the lock-in amplifier. Reducing the probe intensity will also make it possible to increase the Sensitivity. The best suitable lock-in settings should be found for each setup, since this will vary depending on the measurements performed.

5) Measurements

To connect the lock-in amplifier to the computer, press the [Setup] button twice, so the Address light is led up. The number 8 appears in the display to the right. Use the knob to adjust the Address number to 1. The lock-in amplifier is now ready for pump-probe measurements.

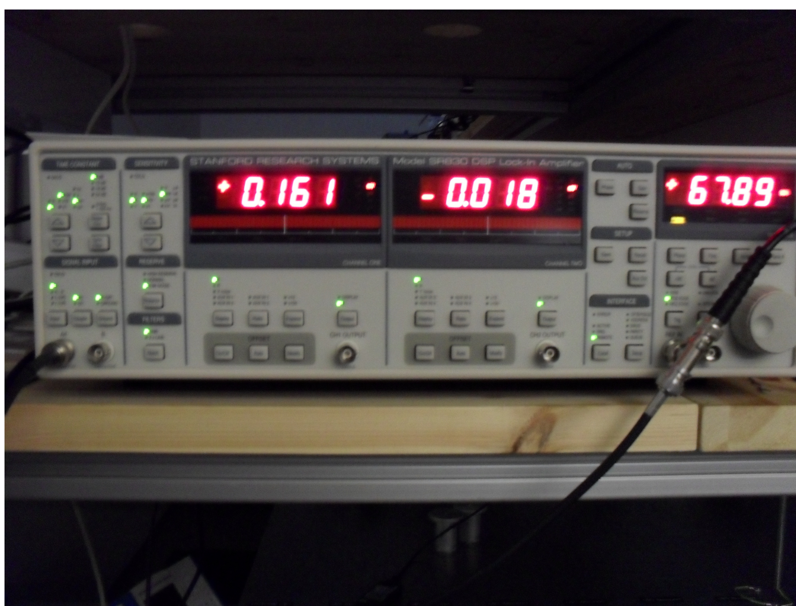

Figure A.1: Shows a picture of the lock-in settings during experiment.

REFERENCES

[1] Standard practice for conversion between resistivity and dopant density for boron-doped, phosphorus-doped, and arsenic-doped silicon. Technical report, American Society for Testing and Materials.

[2] *Optical processes in semiconductors*. Dover Publications, 1971.

[3] M. Strahen G. Maidorn A. Esser, W. Kütter and H. Kurz. Femtosecond transient reflectivity measurements as a probe for process-induced defect silicon. *Applied Surface Science*, 46:446–450, 1990.

[4] I. Abdulhalim. Analytic propagation matrix method for linear optics of arbitrary biaxial layered media. *J. Opt. A: Pure Appl. Opt*, 1:646–653, 1999.

[5] International Energy Agency. Key world energy statistics 2010. 2010.

[6] R. A. Soref B. R. Bennett and J. A. Dek Alamo. Carrier-induced change in refractive index of inp, gaas and ingaasp. *IEEE Journal of quantum electronics*, 26(1):113–122, january 1990.

[7] S. Binetti. Silicon based solar cells: research progress and future perspectives. 2012.

[8] C. Chang P. Yu C. Chen, Y. Lin. Frequency-dependent complex conductivities and dielectric response of indium tin oxide thin films from the visible to the far-infrared. *IEEE journals of quantum electronics*, 46(12), 2010.

[9] T. Y. Choi and C. P. Grigoropoulos. Plasma and ablation dynamics in ultrafast laser processing of crystalline silicon. *Journal of Applied Physics*, 92(9), 2002.

[10] F. E. Doany and D. Grischkowsky. Measurements of ultrashort hot-carrier relaxation in silicon by thin-film-enhanced, time-resolved reflectivity. *Applied Physics Letter*, 52(1):36–38, 1988.

[11] W. C. Sinke F. M. Schuurmans, J. Schmidt and A. G. Aberle. A comparative study between light-biased mw-pcd and mfca measurements on high-quality surface passivated silicon wafers.

[12] B. Gorka. *Hydrogen Passivation of Polycrystalline Si Thin Film Solar Cells*. PhD thesis, Technical University of Berlin, december 2010.

[13] L. Leine H. Bergner, V.Brückner and M. Supianek. Reflectivity and transmittance investigations of photoexcited charge carriers in silicon in the picosecond time domain. *Applied Physics*, A(43):97–104, 1987.

[14] P. Hannaford, editor. *Femtosecond laser spectroscopy*. Springer, 2005.

[15] V. K. Thorsmøller J. C. Brauer and J-E. Moser. Terahertz time-domain spectroscopy study of the conductivity of hole-transporting materials. *Chimia*, 63:189–192, 2009.

[16] T. Jeon and D. Grischkowski. Nature of conduction in doped silicon. *Physical Review Letter*, 78(6):1106–1109, 1997.

[17] J. T. Yates Jr. Surface chemistry of silicon-the behaviour of dangling bonds. *Journal of Physics: Condensed Matter*, 3:143–156, 1991.

[18] C. Kittel. *Introduction to Solid State Physics*. John Wiley and Sons, 2005.

[19] D. Macdonald and A. Cuevas. Trapping of minority carriers in multicrystalline siliocn. *Applied Physics Letters*, 74(12):1710–1712, 1999.

[20] M. Naftaly and R. Dudley. Methodologies for determinding the dynamic ranges and signal-to-noise ratios of terahertz time-domain spectroscopy. *Optics letter*, 2009.

[21] J. Nelson. *The physics of solar cells*. Imperial College Press, 2003.

[22] Newport Corporation, www.newport.com. *Solstice User Manual*.

[23] M. C. Nuss and J. Orenstein. *Topics in Applied Physics*, volume 74, chapter 2 Terahertz time-domain spectroscopy. Springer, 1998.

[24] A. Othonos. Probing ultrafast carriers and phonons dynamics in semiconductors. *J. Appl. Phys*, 83, 1998.

[25] I. H. Libon U. Lemmer N. E. Hecker P. U. Jepsen, W. Schairer. Ultrafast carrier trapping in microcrystalline silicon observed in optical pump-terahertz probe measurements. *Applied Physics Letters*, 79(9):1291–1293, 2001.

[26] R. P. Prasankumar and A. J. Taylor, editors. *Optical Techniques for Solid-State Materials Characterization*. CRC Press, 2011.

[27] J. Ye S. T. Cundiff and J. L. Hall. Optical frequency synthesis based on mode-locked lasers. *Review of scientific instruments*, 72(10), 2001.

[28] A. J. Sabbah and D. M. Riffe. Measurements of silicon surface recombination velocity using ultrafast pump-probe reflectivity in the near infrared. *Journal of Applied Physics*, 88(11):6954–6956, 2000.

[29] A. J. Sabbah and D. M. Riffe. Femtosecond pump-probe reflectivity study of silicon carrier dynamics. *Physics review B*, 66, 2002.

[30] B. E. A. Saleh and M. C. Teich. *Fundamentals of photonics*. •, 2007.

[31] J. H. Scofiel. Frequency domain describtion of a lock-in amplifier. *American Journal of Physics*, 62(2), 1994.

[32] J. Shah. *Ultrafast Spectroscopy of Semiconductors and Semiconductor Nanostructures*, volume 115. Springer, 2nd ed. edition, 2010.

[33] S. L. Shapiro. Ultrashort light pulses. *Topics in Applied Physics*, 18, 1977.

[34] Standford Research System. *About lock-in amplifiers*. 3.

[35] B. .G. Streetman and K. Banerjee. *Solid state electronic devices*. Pearson Prentice Hall, 2000.

[36] R. L. A. Timmer. *Molecular reorientation and transport in liquid and water*. 2009.

[37] L. Titova and F. Hegemann. Some wafers are removed and then remeasure several times, while some only were measured in then same wafer position without setup changes. *La physique au Canada*, 65(2), 2009.

[38] J. Twidell and T. Weir. *Renewable Energy Resources*. Taylor and Francis, 2006.

[39] Z. L. Wang W. Zhou, editor. *Scanning Microscopy for Nanotechnology*, chapter 2 Electron Backscatter Diffraction (EBSD) Technique and Materials Characterization Examples, page 522. Springer, 2007.

[40] A. M. Weiner. *Ultrafast Optics*. Wiley, 2009.

[41] R. Wolfson. Lock-in amplifier: A student experiment. *American Journal of Physics*, 59(6), 1991.

[42] F Wooten. *Optical properties of solids*. Academic Press, Inc., 1972.